Title
Clamped accelerating structures for the generation of high brightness electron beams.

Permalink
https://escholarship.org/uc/item/0zr0k9s9

Author
Pirez, Eylene

Publication Date
2017

Peer reviewed|Thesis/dissertation

University of California
Los Angeles

Clamped accelerating structures for the generation of high brightness electron beams.

A dissertation submitted in partial satisfaction
of the requirements for the degree
Master of Science in Physics.

by

Eylene Pirez

2019

Abstract of the Dissertation

Clamped accelerating structures for the generation of high brightness electron beams.

by

Eylene Pirez

Master of Science in Physics.
University of California, Los Angeles, 2019
Professor Pietro Musumeci, Chair.

This dissertation will illustrate the design, theory and fabrication of a new generation of radiofrequency (RF) photoinjector aimed at obtaining significant improvements in beam brightness, through an innovative accelerating cavity design, with minimized RF breakdown rates and a novel fabrication technique. The UCLA 1.4 cell RF photoinjector has been inspired by the SPARC (LNF-INFN, Italy) 1.6 cell RF electron gun currently operating in the Pegasus beamline. Using the clamping technique with the INFN proprietary-design gaskets, the fabrication for the 1.4 cell photoinjector the INFN can be completed without any brazing process. Careful rounding of all the inside surfaces allows better management of the pulsed heating temperature rise that largely contributes to the rf breakdown limits of older generations of high gradient electron guns. Finally, the clamping technique and innovative gasket design offers a lower risk assembly and lower fabrication costs.

The UCLA 1.4 cell rf electron gun has been designed to operate at a 120MV/m gradient and an optimal injection phase of 70° in order to increase the extraction field experienced by the electrons at photo-emission by a factor of 1.9 compared

to the one in the standard 1.6 cell design running at the same peak field. The maximum achievable beam brightness in a RF photogun depends on the extraction field with a scaling which differs for the various regimes of operation (cigar, pancake, blowout). Nevertheless, for all cases, improving the extraction field improves the beam brightness at least linearly regardless of operating regime.

From the electromagnetic point of view the gun presents a large mode separation, an extra pumping port for dipole moment compensation, a racetrack full cell geometry for quadrupole moment compensation, strongly rounded elliptical iris and coupler for minimal pulsed heating. The electron gun has also been designed to be compatible with several cutting edge experiments. The inclusion of oblique incidence laser ports allows for short focal length laser illumination on the cathode to generate ultra-low emittance bunches as demonstrated in recent experiments. The new photoinjector is also compatible with a load-lock chamber to test advanced photocathodes, such as alkali antimonide cathodes. These promising materials have yet to be tested in high gradient accelerating cavities due to the lack of an ultra-high vacuum (UHV) storage system that is capable of loading cathodes into the injector without breaking vacuum.

The clamping technique has proven useful in the assembly of accelerating cavities. In the last chapter of this thesis, we will also discuss the design and use of the clamping method in the realization of an X-band deflecting cavity that will play a role in the future ultrafast electron diffraction (UED) experiments at UCLA. The goal of the new deflecting cavity is to develop an innovative, inexpensive and low energy UED system that provides short bunches and offers improvements in the temporal resolution of ultrafast electron diffraction measurements.

The dissertation of Eylene Pirez is approved.

Troy A. Carter
James Rosenzweig
Pietro Musumeci, Committee Chair.

University of California, Los Angeles
2019

To my family and friends whose without constant love and support I would have finished this thesis in half the time...

Table of Contents

List of Figures

List of Tables

ACKNOWLEDGMENTS

(Acknowledgments omitted for brevity.)

CHAPTER 1

Introduction

Normal-conducting high gradient RF photoinjectors are widely considered to be the state-of-the-art in terms of electron sources for high brightness beam generation. Due to their characteristics rf photoinjectors have the potential to generate higher quality beams than lower energy/lower gradients photoinjectors based on constant accelerating field (DC photoinjectors) or lower gradient sources (VHF or SRF guns). Their main advantage is the ability to quickly accelerate electron beams to relativistic energies and that the photoemitted beam is generated in a region of very high accelerating field. The current generation of high gradient RF guns is based on the 1.6 cell rf photoinjector which was brought into play during the development of SASE X-ray FEL [1].

1.1 History of RF photoinjectors

The first radiofrequency photoinjector was developed in 1985 in Los Alamos National Laboratory (ANL) as the electron source for an Free Electron Laser (FEL) experiment [2]. The experiment used a Cs_3Sb cathode located in an S-band RF cavity operating at 1.3GHz to produce 12nC bunches[3]. The setup quickly demonstrated the large improvements in beam quality compared to thermionic emission when using a photoinjector. The number of accelerator beamlines using photoinjectors grew quickly with over 20 RF photoguns in operation by 1990. The photoinjectors dominated over thermionic guns due to their ability to achieve much lower emittance and higher current densities.

Normal conduction RF photoinjectors have historically played a large role in linear accelerator facilities and have therefore been considered as sources for linear collider (for example see the Compact Linear Collider (CLIC) design at CERN) or for any other applications of linear accelerators (such as free-electron laser, ultrafast electron diffraction or microscopy, inverse compton scattering, etc.)[4][5][6][7].

The most notable application of high brightness beams has been the X-ray Free Electron Laser (FEL). A typical X-Ray FEL consists of en electron accelerator followed by an undulator or wiggler. X-ray FELs are capable of producing ultra-brilliant laser pulses in the X-ray which can be used to resolve structures and ultrafast dynamics of matter on the atomic scale and creating motion pictures at the femtosecond rate[8]. Because the quality of the X-ray pulses is directly related to the quality of the electron beams injected into the undulators, the needs of X-ray users from numerous scientific fields, such as physics, chemistry, materials science, biology, and life science, have driven the push for better electron beam generation.

The first hard X-ray FEL ,the Linear Coherent Light Source (LCLS), at SLAC ushered a new era of X-ray science in 2009[9]. The second FEL that was put in operation was located at the Japanese SACLA laboratory in 2012 [10]. Notably this machine does not use an RF photoinjector but a DC gun. This is an exception as all other XFELs that have been built or that are being designed so far are based on the use of high gradient RF photoinjectors. Two other XFEL projects began operation in Korea (PAL) and Switzerland (SwissFEL) in 2016. Fig. 1.1 shows some of the great achievements of the field [8]

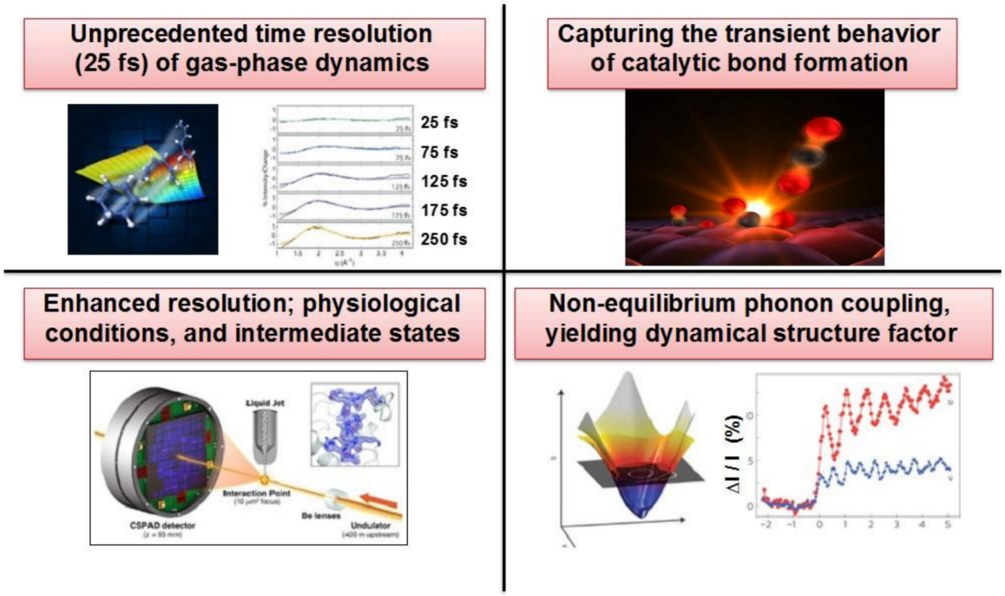

Figure 1.1: XFEL achievements. (top-left) Imaging molecular motion courtesy of SLAC. (top-right) Reaction sequence for catalytic Co oxidation on Ru surface courtesy of SLAC. (bottom-left) LCLS serial crystallography and model of the interface between synaptotagmin-1 and neuronal SNARE complex at SLAC. (bottom-right) Coherent phonon-phonon correlations and acoustic phonon dispersion function (inset) measured in bulk Ge via Fourier transform inelastic X-ray scattering.

The European XFEL (EuXFEL) at the DESY laboratory in Germany launched in 2017. Using superconducting accelerator technologies, the EuXFEL aims to exceed LCLS average brightness at $1\mathring{A}$ by more than 1,000-fold. LCLS II, the next generation facility at SLAC, will also adopt superconducting accelerator technology and tunable magnetic undulators that will support the latest technologies to qualitatively change the way x-ray imaging will be performed [11]. It should be noted that due to the high repetition rate requirements of the next generation of XFELs being developed it is unlikely that high gradient RF photoinjectors will be used since these are currently limited in repetition rate. In fact, one of the main open challenges in the design of these machines is the development of a suitable electron source.

Another application that demands high brightness electron sources is the transmission electron microscope (TEM). TEM is a very powerful tool in many areas of research. In the past decades, many improvements have been made in the spatial resolution. With the introduction of spherical and chromatic aberration correction methods that have allowed reaching sub-Anstrom resolution. [12]. Perhaps one of the last remaining drawbacks of these machines is that in order to capture a high resolution micrograph one needs to use exposure times of milliseconds to seconds due to the limited electron current. Efforts to bring the same advancements into temporal resolution are ongoing. In particular higher beam brightness is needed from the source in order to increase the electron current in the electron optic column and acquire the same image in a shorter amount of time. At high current levels, the limits in spatial and temporal resolution will be set by electron-electron interactions, suggesting the use of relativistic electrons to suppress space charge forces. [13] . Initial experiments in time-resolved transmission electron microscopy at TU-Berlin have demonstrated down to 10ns temporal snapshots with a few hundred nanometers spatial resolution [14].The Dynamic transmission electron microscopy (DTEM) in Livermore National Laboratory has achieved single-shots at 10-ns temporal resolution with 19-nm spatial resolution [15]. Even though most of these experiments have used modified DC guns a clear opportunity exists to greatly extend the range of possibilities in ultrafast electron diffraction and microscopy using such high brightness electron source and a number of research efforts have been directed towards the use of RF photoinjectors for this application[13][16].

These examples motivate further research in improving the quality of the electron beams from RF photoinjectors, which is the goal of this thesis.

1.2 Elements of a Normal Conducting RF Photoinjector.

A generic photoinjector system consists of an electron source, based on photoemission process from a cathode surface. The initial accelerating field region is followed by an focusing lens whose main function is to match the beam for immediate application or more commonly into a subsequent accelerating section as shown in Fig. 1.2 [17]. The details of this matching are particularly important when space charge effects dominate the beam dynamics and give rise to the emittance compensation theory [18] [19].

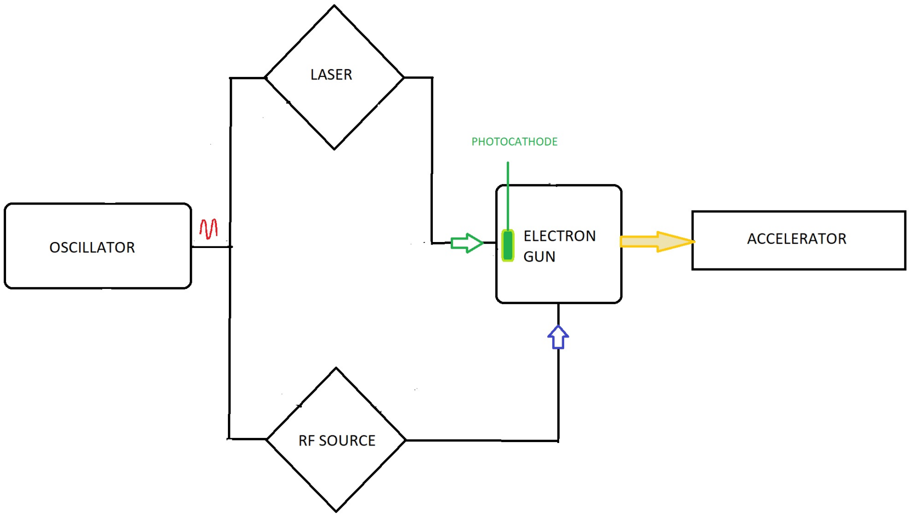

Figure 1.2: Schematic of main components of photoinjector systems.

The use of the laser system to generate the electrons at the cathode is one of the characteristics of RF photoinjectors and allows controlling the beam properties by tailoring the laser pulse prior illumination of the photocathode. For example, the number of electrons emitted depends on the intensity of the incident laser. The quantum efficiency (QE) of the photocathode at the specific laser wavelength is defined as the ratio of the number of electrons generated over the numbers of impinging photons and depends on the choice of the cathode material. For copper this number is typically around 10^{-5}.

The other important characteristic of a photocathode is the MTE (mean transverse energy). This quantity is associated to the transverse angular spread of the electrons as they are photoemitted and as we will see later it ends being one of the limit to the maximum achievable brightness from photoinjectors. The duration of the photoemission can be controlled by varying the laser pulse length. For very high emitted charges, the self-field of the beam can inhibit further emission. The duration of the laser pulse is typically only few degrees of radiofrequency phase (it can be much shorter than that). Since the evolution of the beam is strongly influenced by the fields felt by the particle at photoemission, it is not surprising that a characteristic challenge in these systems is the complexity of timing and synchronization systems between the RF and the laser system,

Another important component of RF photoinjectors is the coupling method of the RF power into the electron gun. Variations exist but a popular method is using a hole in the side-wall of one of the cavities for coupling into the structure and using an on axis iris to couple from cell to cell within the structure.

1.3 RF Accelerating Cavities

As mentioned earlier, RF photoinjectors are preferred over DC gun because of their ability to support higher accelerating fields which tends to minimize the emittance growth. It is therefore useful here to review the basic of radiofrequency resonant cavity theory. The simplest approach to discuss RF cavity theory is to begin with a pillbox cavity geometry of radius R, and length d, as shown in Fig. 1.3 [20].

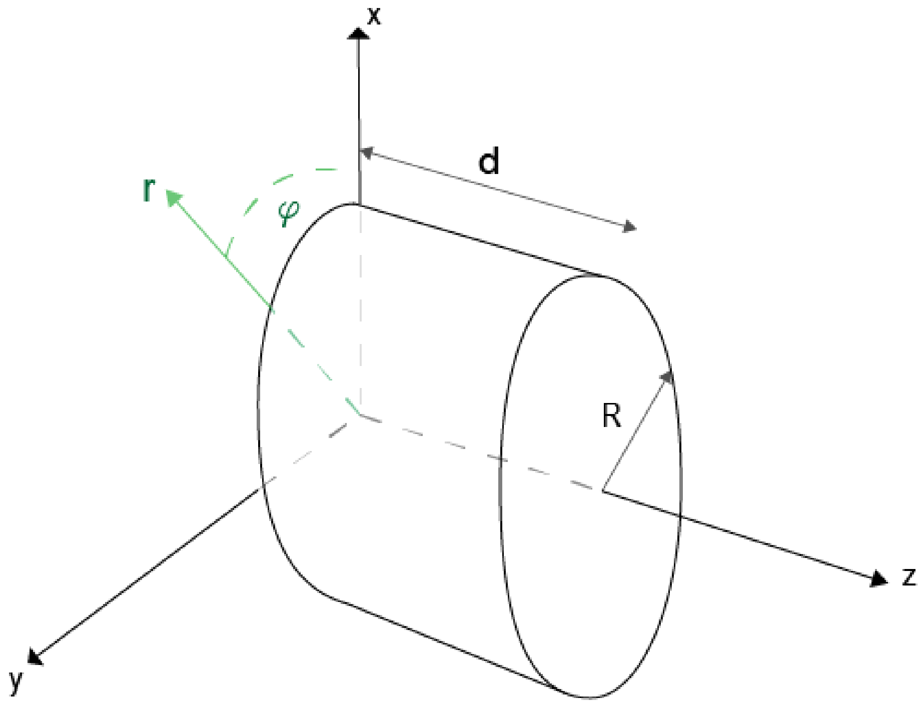

Figure 1.3: Pillbox cavity.

The longitudinal component of the electric field for a transverse magnetic (TM) mode for a pillbox with perfectly conducting walls containing a lossless medium, in our case it will be vacuum with ϵ_0 and μ_0 dielectric and magnetic permitivities, is given by

$$E_z(r, \varphi, z, t) = E_0 J_m(k_{mn} r) cos(m\varphi) cos(p\pi \frac{z}{d}) cos(\omega t), \tag{1.1}$$

where J_m is the m-th Bessel function, $k^2 = \epsilon\mu\omega^2 - p^2\pi^2/d^2$ and ω is the angular frequency. The modes of the cavity are indexed by m, n and p. Applying boundary conditions at R, we enforce $E_z(R, \varphi, z, t) = 0$. RF accelerating cavities typically operate in the TM_{010}, transverse magnetic. In our case where $m = 0$ and $n = 1$, the first root of $J_0(x)$ occurs at $x_{01} = 2.1405$.

We can calculate the resonant frequency ω_0 for a TM_{mnp} mode using

$$\omega_{mnp} = \frac{1}{\epsilon\mu}\sqrt{\frac{x_{mn}^2}{R^2} + \frac{p^2\pi^2}{d^2}} \tag{1.2}$$

For example, a cylindrical cavity operating in mode T_{010} with a radius of 40.18mm has a resonance frequency of 2.856GHz.

The RF photoinjector consists of a series of cells. Typically, the cathode is embedded (it is one of the walls) in a short cell, followed by one or more full cells of length $\lambda/2$. When N cells are used in the structure, coupled oscillator theory indicates that a number N of fundamental modes exist. In order to synchronously accelerate electrons the entire structure typically is operated in the π mode which is the one for which the sign of the longitudinal electric field changes by π over the length of a cell. The fields of the π mode oscillate at the same frequency, ω, but with opposite sign which is the reason this mode is useful in accelerators. The sign-changing field allows the electron bunch to catch up and remain synchronous with the accelerating RF field. Extra cells can be added to increase the output energy [17].

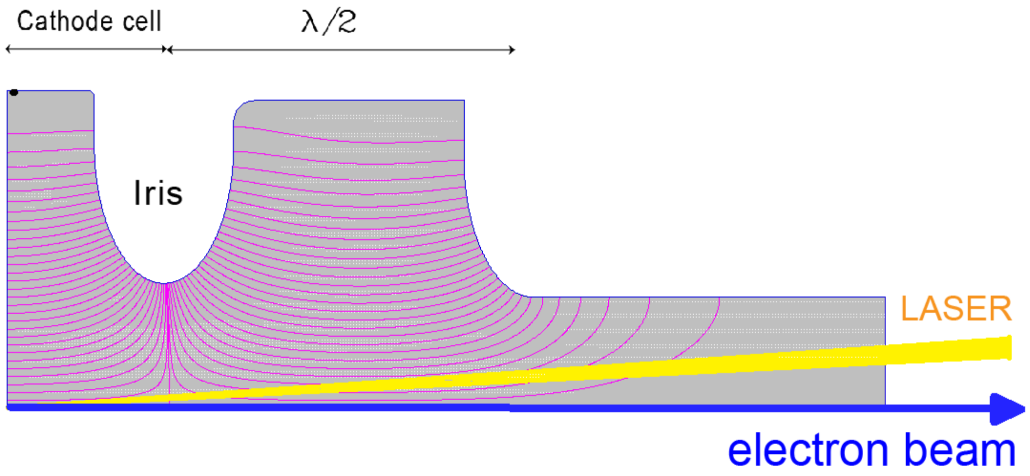

Figure 1.4: Example of RF cavity schematic.

RF cavities are not lossless systems in practice as they do not have perfectly conducting walls. Power in an RF structure typical flows as shown in figure 1.5.

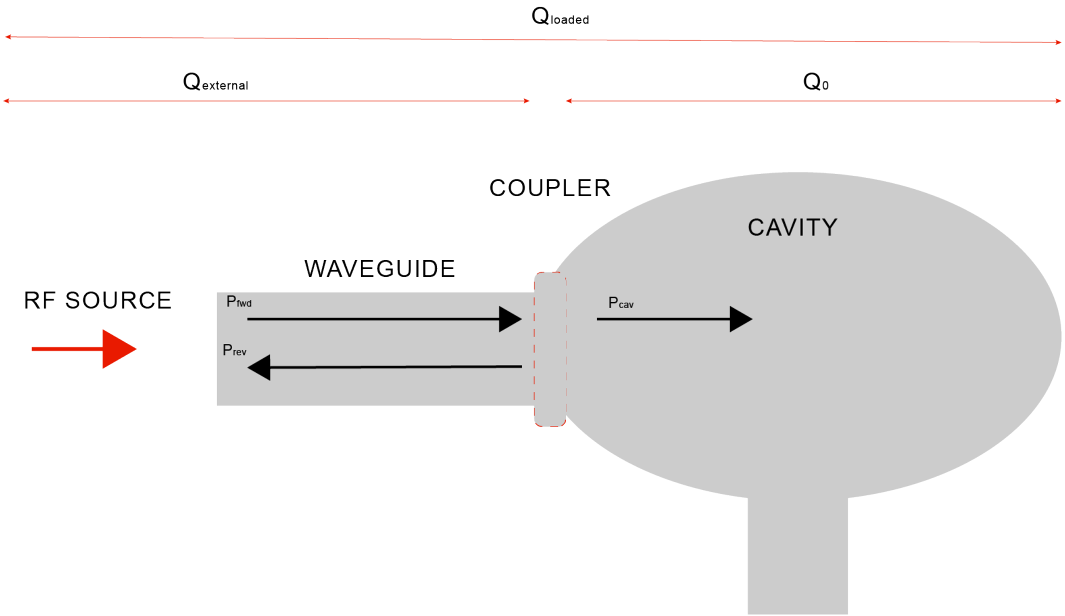

Figure 1.5: Power flow and quality factor 'Q' schematic in a typical rf cavity.

There are a variety of power coupling methods such as connecting the waveguide to the cavity side wall or using a coaxial RF feed with a transformer. Using the side wall is perhaps the most common method. This side-wall method can introduce asymmetries in the cavity that that affect the quality of the beam. We will discuss on how to compensate for these effects in the upcoming chapter.

The RF power in the system, internal and external, depend on various parameters. One important RF design parameter is the quality factor, Q, which is given by

$$Q_{external} = \omega_0 \frac{U_{stored}}{P_{external}} \tag{1.3}$$

where U_{stored} is the energy stored in the cavity, ω_0 is the resonance frequency, and $P_{external}$ is the energy loss through the coupling hole per RF cycle. Similarly, we can look at the power losses in the cavity in steady-state.

$$P_{cav} = \omega_0 \frac{U_{stored}}{Q_0} \tag{1.4}$$

The quality factor of the entire system takes into account both the losses through the coupler and through the cavity walls and is called the loaded Q, Q_L. It is expressed in terms of the other quality factors as

$$\frac{1}{Q_L} = \frac{1}{Q_0} + \frac{1}{Q_{external}} \tag{1.5}$$

.

Combining these two equations, we can define the coupling parameter, $\beta_{coupling}$.

$$\beta_{coupling} = \frac{Q_0}{Qexternal} \tag{1.6}$$

When the RF power is turned on, there are transients whose time-dependence is determined by the cavity response time. This is known as the cavity filling time. For a steady state cavity, the coupling parameter determines this filling time. The goal for the RF power system is to generate a pulse long enough to fill the cavity so that the electrons can be injected at the highest possible fields.

$$\tau_{cav} = \frac{2}{\omega_0} \frac{Q_0}{1 + \beta_{coupling}} \tag{1.7}$$

There are 3 possibilities for the coupling coefficient. For a $\beta_{coupling} < 1$, the system is considered "undercoupled" and there is always a finite reflected power. Critical coupling corresponds to a $\beta_{coupling} = 1$ for which the steady-state reflected power, P_{rev}, becomes zero. If $\beta_{coupling} > 1$, the system is "overcoupled". In this case, the transient reverse power goes to zero quickly but then increases again with time.

1.4 Emittance and Beam Brightness.

The photoinjector main task is to produce the highest quality beam achievable. Two terms that are commonly used to measure the beam quality are emittance and brightness. The emittance is the area or volume of phase space the electrons occupy. The six dimensional phase space is the one formed by an electrons three positions (x,y,z) in the cartesian coordinate system and momenta, (p_x,p_y,p_z). An electron beam (composed by N electrons) will be fully characterized by a distribution function in the 6D phase space, which unfortunately can not easily be measured in the experiments. In practice, we can only measure projections of the 6D phase space onto the 2D trace spaces (xx', yy' and zz') where the angles are normalized by the total beam momentum. Therefore, $x' = \frac{p_x}{p_{total}}$, where $p_{total}^2 = p_x^2 + p_y^2 + p_z^2$. The second moments of the beam distribution are often used in literature in expressions regarding the beam properties. For example, the root mean square (RMS) size of the beam is defined as $\sigma_x^2 = \langle x^2 \rangle$. The RMS divergence can be expressed as $\sigma_{x'}^2 = \langle x'^2 \rangle$. These two rms quantites can be correlated if a $\langle xx' \rangle$ term is present and different than 0. In two dimensions we can defined a phase space area occupied by the beam as the root mean square (RMS) normalized emittance defined as,

$$\epsilon_n = \beta\gamma\sqrt[2]{\sigma_x^2\sigma_{x'}^2 - \sigma_{xx'}^2} \tag{1.8}$$

where $\beta = \frac{v}{c}$ is the electron velocity normalized to the speed of light and $\gamma = \frac{E_{total}}{mc^2}$ is the total beam energy, E_{total}, normalized to the electron mass.

The transverse beam brightness is a parameter that involves the emittance and the peak current, I_{peak}, which is how much charge per unit time there is in a pulse. Beam brightness was initially introduced by Ruska in the development of the first transmission electron microscopes to rank how well we can focus the beam[21]. There are many expressions for beam brightness found in literature but the true figure of merit is the 6D beam brightness,

$$B_{6D} = \frac{N_e}{V_{6D}} = (\frac{m_0 c}{\pi})^3 F \frac{Q}{\epsilon_{nx}\epsilon_{ny}\epsilon_{nz}} \tag{1.9}$$

where N_e is the number of electrons, V_{6D} is the 6D volume in phase space and can be related to commonly used quantities such as charge and emittance. The 6D beam brightness is one of the fundamental invariant in beam physics due to the Liouville theorem, but its use is hindered in practice due to the difficulties of measuring the longitudinal phase space. Liouville theorem states that if all elements in a beamline can be described by Hamiltonian dynamics the 6D phase space density will remain constant throughout the system.

It is interesting to note that there is a fundamental quantum limit to the beam brightness. The quantum phase space is defined by Heisenberg uncertainty principle and Pauli exclusion principle allows only two electrons (spin up and spin down) in the same state. Therefore, we can express the maximum achievable beam brightness as follows,

$$B_{quantum} = \frac{2e}{h^3}(m_0 c) = \frac{2e}{(\lambda_c)^3} \tag{1.10}$$

where λ_c is the Compton wavelength. This yields a quantum limited beam brightness of $B_{quantum} = 10^{25} A/m^2$. Even though several improvements in photoinjector design have been made over the years and the beam brightness has significantly increased, the achieved beam brightness is at least five orders of magnitude lower than this theoretical quantum limit for a fully coherent electron source.

It is now useful to review some of the expressions of beam brightness that are commonly used in practice as a function of parameters we can control such as the electric accelerating field, E_o [22].

There are two regimes of operation that are commonly used to generate electron beams in RF photoinjectors: the pancake regime and the cigar regime. The pancake regime is when the beam is very short in the longitudinal direction and can be approximated as an infinitely wide thin disk of charge. The cigar regime is the opposite; long in the longitudinal direction and short in the transverse direction.

The 4D beam brightness could be expressed as the following

$$B_{4D} = \frac{Q}{\epsilon_{nx}\epsilon_{ny}}. \tag{1.11}$$

It is defined as the charge density in the 4D transverse phase space where its' scaling depends on the emitted beam aspect ratio at the cathode. In the pancake regime, the 4D brightness is defined as the charge density in the 4D transverse phase space where the scaling depends on the emitted beam aspect ratio at the cathode. The emission cuts off at the moment the surface charge density (divided by ϵ_0) equals the accelerating field and one can write a limit for the achievable beam brightness as

$$B_{n,4D} = \frac{mc^2\epsilon_0 E_0}{2\pi k_B T} \tag{1.12}$$

where $k_B T$ is the mean transverse kinetic energy resulting from photo-emission (typically on the order of the difference between the photon energy and the cathode work function). In the cigar regime, the beam is sufficiently long such that the aspect ratio is unity or larger. The beam can no longer be approximated as an infinite charged plane. As electrons are accelerated away from the cathode, their contribution to the space charge field at the cathode will decrease and the emitted charge in this regime scales as $E_0^{1.5}$.

For FEL , the 5D brightness becomes relevant. If we only consider the total bunch charge instead of the electron peak current, the electron pulse length and emittance depend on the electric field. The gain length is defined as the current density in the 4D phase space, and therefore equal to the 4D brightness divided by the pulse length. For cases in which the the space charge field is much lower ($< 10\%$) than the accelerating field, but large enough that it causes strong de-bunching (expansion) of the electron beam the final pulse length depends on the accelerating gradient and the maximum achievable peak brightness scales as E_0^2 [23].

1.5 RF Breakdown Physics and Limitations.

For decades, RF photoinjectors have been the best solution for high brightness beam generation. Several improvements in photoinjector design have been made over the years but, as we saw in the 'Beam brightness' section, there is a lot of room for improving the achievable beam brightness.

One of the biggest limiting factors in RF photoinjectors is a phenomena known as RF breakdown. Physically, RF breakdowns are events during operation where within sparks occur within the structure. These are accompanied by large rises in dark current, high vacuum levels and disruptions in the RF reflected signals. Understanding the exact mechanism of the RF breakdown rate is still a work in progress but reproducible behavior sheds light into solutions that can be adopted. A recent graduate from our laboratory Dr. Alex Cahill focused his Ph.D. work in the study of these problems and in what follows we summarize some of his conclusions.

The current consensus is that RF breakdowns are caused by deformations and movement of dislocations in the metal bulk when exposed to large surface RF electric and magnetic fields.

RF structures operate with large electric fields and these fields generate currents even in the absence of beam. These currents generated are a result of the fields knocking conducting electrons in the metal to freely propagating states via quantum tunneling[24][25].

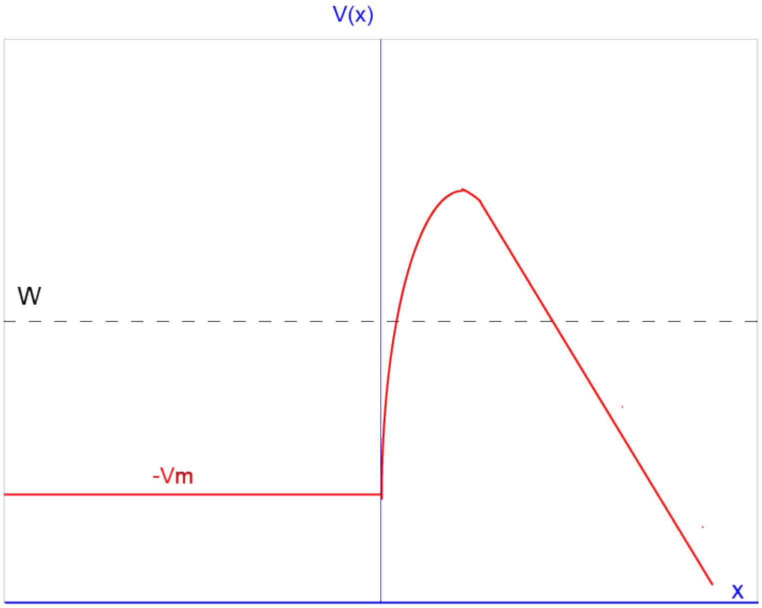

Figure 1.6: (a) Potential barrier.

If we were to model the surface as a semi-infinite sheet, we can write the potential barrier as

$$V(x) = -V_m, \quad x \leq 0 \tag{1.13}$$

$$V(x) = -eEx - \frac{e^2}{16\pi\epsilon_0 x}, \quad x > 0 \tag{1.14}$$

The probability of undergoing quantum tunneling can be found using the semi-classical WKB approximation assuming the electrons in the metal have a Fermi-Dirac distribution such that

$$dn = \frac{2V_e}{h^3}\frac{dp_x dp_y dp_z}{e^{\frac{W-\zeta}{k_B T}} + 1} \tag{1.15}$$

for momentum, p, and energy, W.

The Fowler-Nordheim equation has been adapted to RF structures to predict these currents, $J_{FN} \propto E^{2.5}$, over a single period. The strong dependence on the electric field tells us that the higher the fields, the larger these currents are which increase the RF breakdown probability.

A study was conducted at SLAC which monitored the RF breakdowns with different types of RF photoinjector copper treatments and properties.Typically, RF photoinjectors tend to be braized or heat treated, which turns the metal 'soft' and makes it more susceptible to these mechanical deformations. As shown in the figure below, harder copper and cavities operating at lower temperatures exhibit lower RF breakdown rates for the same accelerating gradient as softer copper structure.

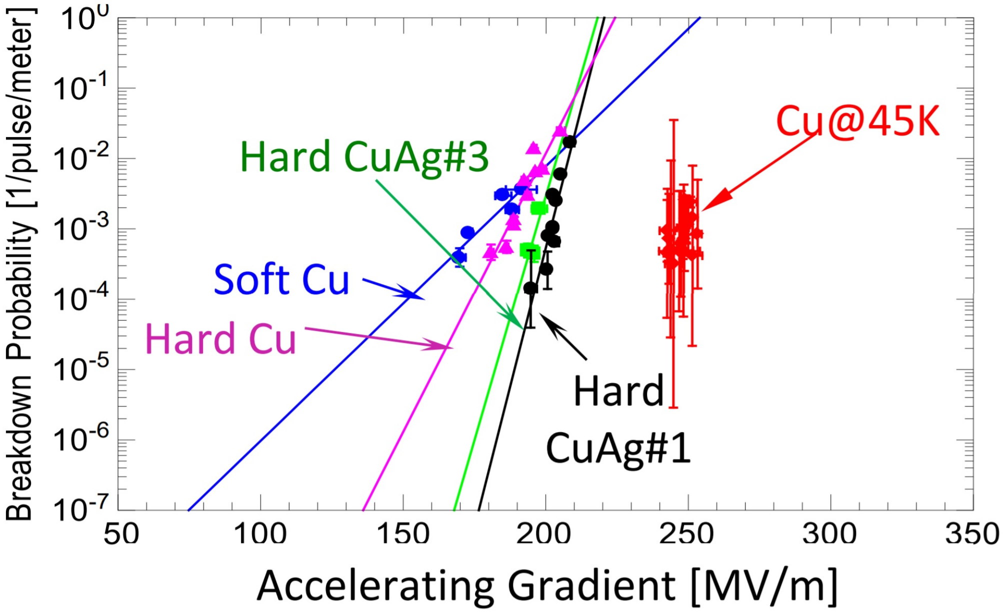

Figure 1.7: RF breakdown study by SLAC using different types of copper.

The breakdown rate (BDR) is experimentally quantified as

$$BDR = \frac{Number\ of\ breakdowns}{Number\ of\ pulses\ x\ Pulse\ length}. \tag{1.16}$$

The initial breakdowns are independent events and trigger more breakdown events. Properly conditioning of the RF structure reduces the initial breakdown. Proper conditioning techniques involves a gradual increase in electric field and slowly reducing pulse length while maintaining a constant RF breakdown rate.

It has been observed that after the RF structure has been properly conditioned, the RF breakdown rate (BDR) is affected by the peak pulse surface heating.

Two experiments at SLAC were designed to test pulsed heating damage on metal disk samples. The first experiment, using a pillbox cavity, showed that cracking can occur in Cu structures when exposed to millions of pulses at above 80 K, showing that pulsed heating can be a significant problem for pulsed high gradient structures. The second experiment used a cavity that was designed such that sample disks were not exposed to any surface electric fields, but had enhanced surface magnetic fields, where the structures were tested with maximum temperature rises of 110 K. All the structures showed visible damage where the pulse heating was the largest. The damage level varied from material to material. The structure made out of the harder materials, such as CuAg and non-annealed Cu alloys, showed significantly less damage [20].

The current research does not explain the microscopic mechanism determining the breakdown rate but approximations can be made to estimate this pulsed heating temperature rise. If we consider a semi-infinite plane of a conductor of finite conductivity under an electromagnetic field, we can write the power dissipation per unit area on the surface as

$$\frac{dP_{cav}}{dA} = \frac{1}{2}R_s(T)|H_{||}|^2 \tag{1.17}$$

where R_s is the RF surface resistance and $H_{||}$ is the magnetic field parallel to the cavity surface. It is important to note that it is assumed that conduction and elasticity are independent of each other. The relationship between them is not yet understood in high gradient structures.

We can find the temperature distribution by using the heat equation,

$$\frac{\partial^2 T(x,t)}{\partial x^2} + \frac{R_s(T)H_{||}^2}{k_c(T)\delta(T)}e^{-2x/\delta(T)} = \frac{1}{\alpha_d}\frac{\partial T(x,t)}{\partial t} \tag{1.18}$$

.

The 1D approximation is derived in detail in [26]. The expression commonly used to approximate the temperature rise assuming a square pulse shape of length, t_p, is

$$\Delta T = \frac{R_s H_{\|}^2 \sqrt{t_p}}{\rho c_\epsilon \sqrt{\pi \alpha_d}} \tag{1.19}$$

.

Minimizing pulse heating temperature rise is tackled by cooling mechanism design and modeling geometries to minimize concentration of surface magnetic fields inside the structure. A popular first-order method to reduce the pulse heating temperature rise is to avoid edges and tightly rounded geometries.

1.6 Thesis organization

The current generation of electron sources have improved tremendously through the development of accelerator, simulation codes, laser and cathode technologies in the last few decades. In this introduction, we have discussed the importance of high gradient photoinjectors for the generation of high brightness beams and their role in key applications like XFEL and time-resolved electron microscopy. We have also seen the theoretical quantum limits of beam brightness which currently stand at 5 orders of magnitude higher than what has been achieved in the laboratory. We have gathered various expressions from the latest research to understand quantities like the extraction field and how it enters the beam brightness in several regimes of operation. We have finally brought into attention the ongoing efforts to understand rf breakdown and the latest efforts to resolve this issue. Even though photoinjectors have reached a very mature stage, there is clearly plenty of room left for improvements in performance.

The goal of this project is to create a new generation of rf photoinjectors that takes advantage of all of these ongoing discoveries and advancements in the field. In this thesis, we introduce the design of a 1.4 cell rf photoinjector. This structure will be the new generation high gradient photoinjector that will operate at the Pegasus beamline at the University of California, Los Angeles (UCLA).

Chapter 2 will be devoted to explaining the theory, design and the engineering of this new generation of electron gun. We will begin by discussing the beam dynamics and the beam properties of the structure which is mainly characterized by much higher extraction fields. We will review and explain the rf and electromagnetic design of the photoinjector which tackles many shortcomings in the previous generation of photoinjectors. The new clamping technique will be reviewed. Adopting this fabrication design eliminates the brazing step and allows for the use of hard copper which has been shown to improve the rf breakdown rate. We will also implement careful rounding of all the surfaces in order to reduce the rf pulsed heating. The structure has been built to exploit the advancements in photocathode technology and we will discuss how its design will allow to test advanced photocathodes amongst others.

Along the design the of the rf photoinjector, new approaches to fabricating accelerating structure have been learned. Chapter 3 will discuss the design and construction of an X-band deflecting cavity that puts into practice these new techniques.

CHAPTER 2

1.4 Cell RF Photoinjector

In this chapter we describe the design of a high gradient 1.4 cell S-band photoinjector developed for operation at the resonant frequency of 2.856 GHz. From the fabrication point of view the gun is built on a novel assembly procedure which does not require the brazing step; from the beam dynamics point of view, the main novelty of the design is a shortened half cell to achieve very high injection field and improve the beam brightness. The chapter is organized as follows. First, we will describe the laboratory facilities and the current photoinjector in use. We will then present the rf and electromagnetic design and the expected improvements in beam parameters. We will also discuss important additions to the design and their applications as well as fabrication method and component testing.

2.1 The Pegasus Laboratory at UCLA

The PEGASUS (Photo Electron Generated Amplified Spontaneous Undulator Radiation Source) at UCLA is a student operated accelerator laboratory under the guidance of professor Pietro Musumeci. It has been built to study high brightness electron beams and develop and test novel accelerator technologies.

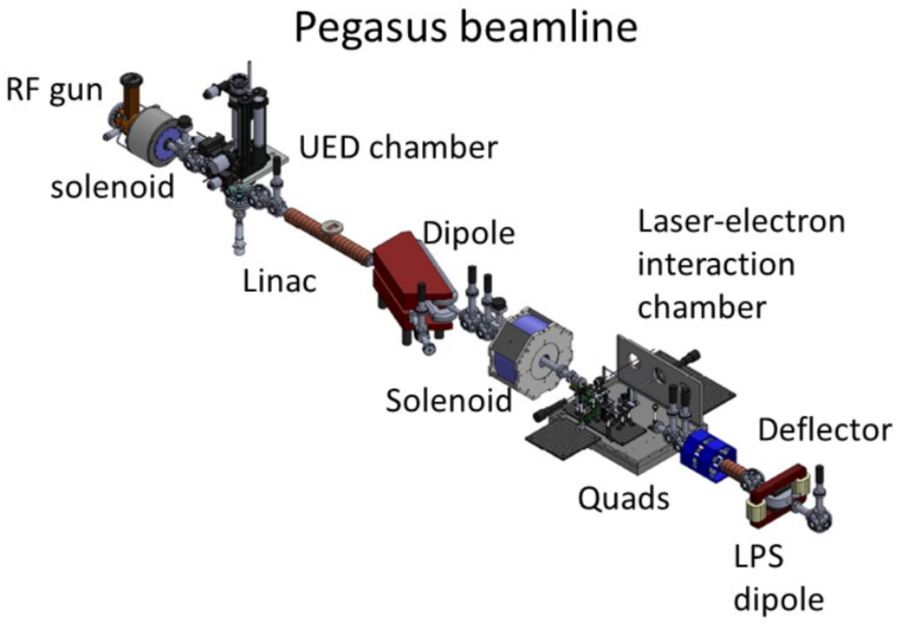

Figure 2.1: Schematic of the Pegasus beamline at UCLA.

The facility is consists of three main rooms: the Pegasus beamline, the laser room and the control room. The Pegasus beamline contains a radiation-shielding bunker with automated door and personnel protection system, control room, RF modulator and klystron (SLAC XK-5, 2856 MHz), high stability HVAC (temperature control) system throughout lab; a solid foundation (located in the subbasement of building on solid bedrock); clean electrical system including locally generated high current 208VAC three phase; and, high flow de-ionized chilled water circuits. The Pegasus rf gun, as of June 2018, is the SPARC 1.6 cell RF photoinjector which we will discuss in detail in the upcoming sections

The laser room is located immediately adjacent to the beamline which gives a short optical path from the laser to the photoinjector. The photocathode drive laser is a state-of-the-art all diode pumped Titanium:Sapphire based system from Coherent. A

79.33 MHz optical train from the master oscillator synchronized with the RF with an active phase locking loop at a level better than 250fs seeds a 1kHz regenerative amplifier. Infrared (800 nm) pulses with energy greater than 3mJ and length less than 35fs are obtained after final compression. The large bandwidth of the Ti:Sapphire allows superior flexibility in adjusting the laser pulse length [27].

Low level rf is produced by a 79 MHz signal which its frequency gets multiplied to the desired frequency of operation. After passing through a phase shifter, the signal is raised to over 1kW by an amplifier. This signal is then used as the rf input for the Pegasus Klystron. A low level rf signal map is shown in fig. 2.2.

2.2

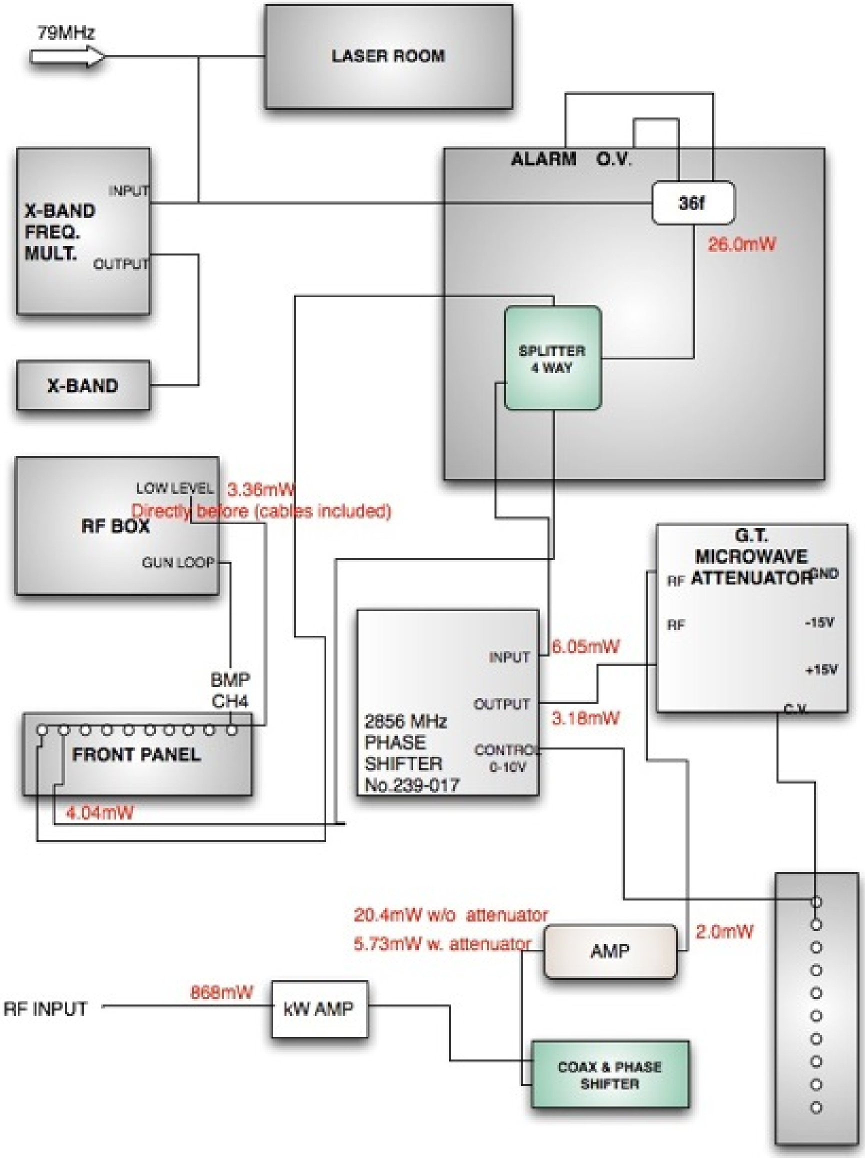

Figure 2.2: Low Level RF components.

Pegasus uses a SLAC XK5 klystron powered by a transmission line 42 kV modulator. Operating at 2.856GHz, it can transport up to 10 MW of electromagnetic power to the accelerator bunker through an SF6 filled high power waveguide line. RF windows isolate klystron vacuum on one end and the linac beamline on the other.

As seen in the schematic 2.1, an emittance compensation solenoid is located right after the beam exit pipe of the rf gun. The LCLS-design solenoid was refurbished from Brookhaven National Laboratory (BNL). A test beamline with vacuum systems, quadrupole optics, steering magnets, insertable beam profile monitors, stripline detectors, and a Faraday cup beam charge collector is in place. Several beam diagnostic stations are set in place capable of measuring beam energy, energy spread, beam charge and other important beam parameters. Beam position and charge is monitored using YAG crystals imaged with CCD cameras.

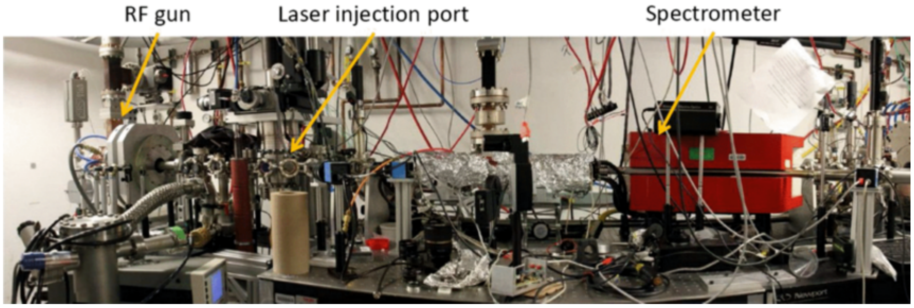

Figure 2.3: Overview of the UCLA Pegasus beamline facility.

The control room of Pegasus contains four Windows PC and three Linux boxes with ISA and PCI cards for Digital IO, ADC, DAC and video are linked together and to a Linux lab central server by Gigabit Ethernet. The operating system has an independent architecture based on PostgreSQL that allows remote operation. Operators use a Labview [28] interface software for operation that has been developed by Pegasus users to closely resemble modern accelerator facilities control systems.

2.1.1 Commissioning the SPARC 1.6 RF gun

The SPARC photoinjector is a 1.6 cell electron gun designed at INFN, Laboratori Nazionali di Frascati, to operate at a gradient of 120MV/m in the S-band. It was designed as a replacement for the SPARC laboratory injector and as a test for the future ELI NP to operate at a resonant frequency of 2.856GHz [29] [30]. It has been commissioned at Pegasus up to a gradient of 95MV/m mostly limited by the available rf power.

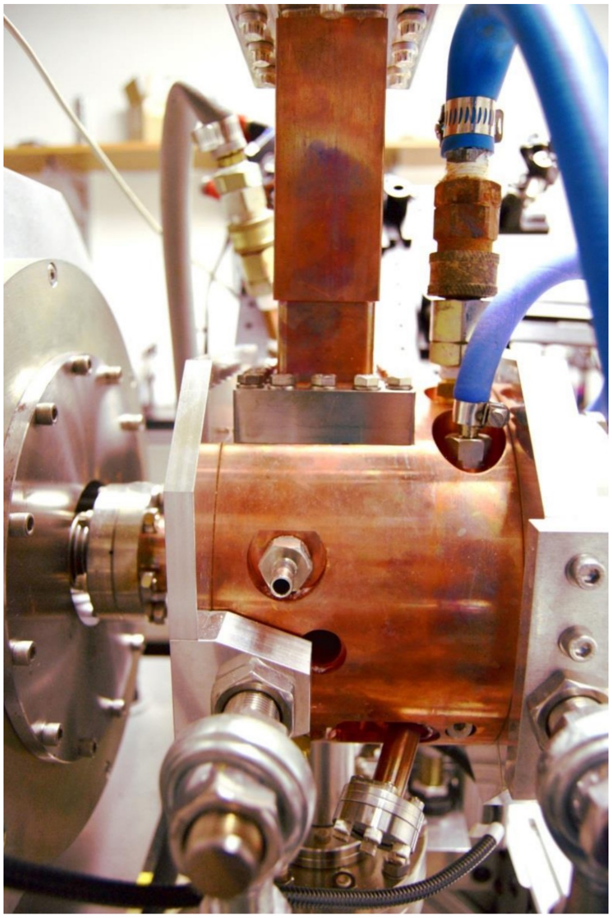

Figure 2.4: The SPARC 1.6 cell photoinjector in the Pegasus beamline.

This particular version of a 1.6 cell gun used a clamping fabrication technique to reduce the rf breakdown. The structure also included several improvements in photogun design such as a dipole moment compensation, large mode separation, short pulse handling, amongst others. The UCLA Pegasus beam line was the laboratory chosen to commission this new structure. The SPARC replacement photoinjector was successfully installed in 2016 and remains in operation in 2018. The structure underwent low power testing, high power testing and several weeks of conditioning before full operation [31].

In Fig 2.5 (a), the main components of the SPARC gun are shown un-clamped consisting of the cavity machined out of a single piece of oxygen free copper that has never undergone any heat treatment, a cap, a copper cathode, and a radio-frequency and vacuum gasket designed and patented by INFN that seals the cavity and cap when clamped together [32]. Before the final clamping, the gun has been cleaned with a detergent (ALMECO-19) and a mixture of organic (citric) acid and distilled water, in a bath with an ultrasound machine. In Fig. 2.5 (b) the installed and clamped structure is shown at the Pegasus beamline. After the assembly, the structure underwent a bake-out at 150° for 24 hours allowed reaching a vacuum pressure below 5×10^{-10} mbar.

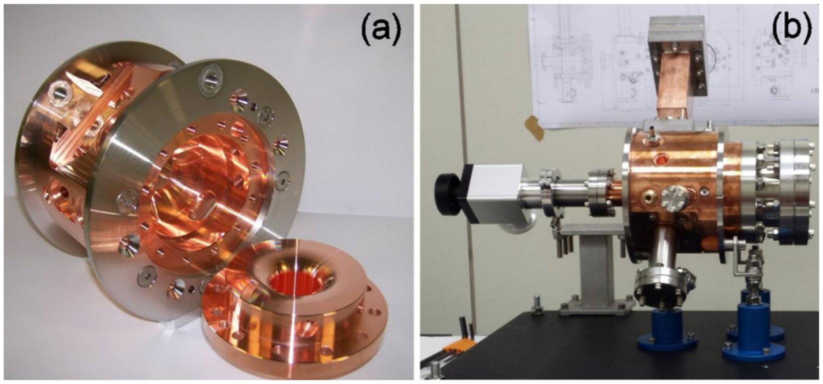

Figure 2.5: (a) Unclamped SPARC 1.6 electron gun. (b) Clamped and installed SPARC gun at the Pegasus laboratory at UCLA.

The low RF power test was done using a network analyzer and the bead-drop technique. The bead-drop or bead-pull technique consists of a small dielectric or metallic bead is pulled through a cavity to while measuring the RF via a Network analyzer. This procedure tells us the field distribution inside the resonant structure which allows understanding the field flatness between the different cells. The accelerating field profile after tuning is shown in Fig. 2.6 (left).

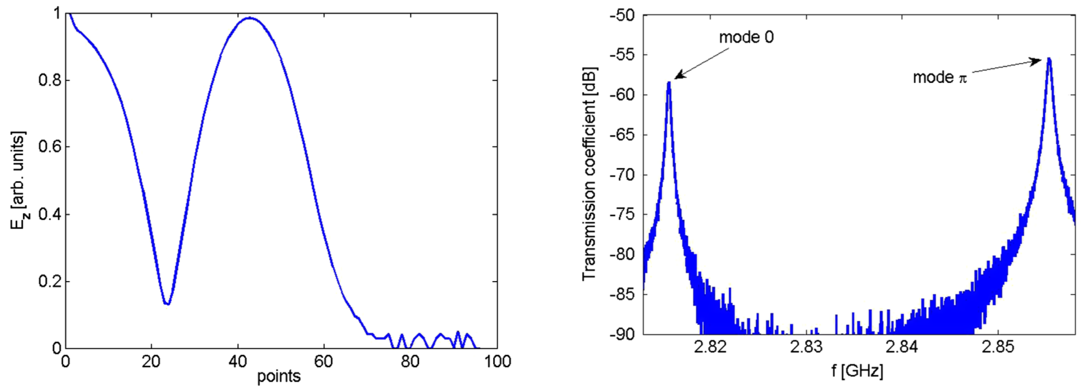

Figure 2.6: (left) Measured accelerating field of SPARC gun. (right) Measured mode separation between the 0-mode and the π-mode of SPARC.

For low rf power characterization of high frequency circuits, we use scattering parameters. The gun is equipped with a weakly coupled (-64 dB) port which looks directly at the fields in the full cell. S-parameters model the structure as a simple network. In our case, the photoinjector is modeled as a 2 port network. The S-parameters relates the transmitted or reflected waves to the incident waves.

$$\begin{pmatrix} b_1 \\ b_2 \end{pmatrix} = \begin{pmatrix} S_{11} & S_{12} \\ S_{21} & S_{22} \end{pmatrix} \begin{pmatrix} a_1 \\ a_2 \end{pmatrix} \tag{2.1}$$

$S_{11} = \frac{b_1}{a_1}$ is the reflection coefficient we commonly use because it is the ratio of the wave amplitude coming out at the chosen port to the wave incident at that port. $S_{21} = \frac{b_2}{a_1}$ is the transmission S-parameter and is the ratio of the wave coming out of a different port than was incident wave port [33].

Figure 2.7: S-parameters for transmission and reflection power measurements schematic.

We search for the cavity modes by looking for peaks in the S_{11} parameter scan. The 0-mode and the π-mode resonance frequencies can be seen in Fig. 2.6 (right). An RF structure is considered to have balanced fields when the peak field in each of the cell have the same magnitude for the π-mode. Taking measurements for the 0-mode and the π-mode resonances as a function of bead position reveals the shape of each mode in the gun. A mode separation of 40MHz is shown with the π mode at 2.856GHz. The S_{11} reflection coefficient, Γ, of the π mode after tuning is shown in Fig. 2.8.

$|\Gamma|$ is defined depending on the coupling scenario. Three types of coupling exist: undercoupled ($\beta_{coupling} < 1$), critical coupling ($\beta = 1$) and overcoupled ($\beta > 1$). The reflection coefficient is measured in decibels and give us the coupling beta using the following expressions.

$$|\Gamma| = \frac{1 - \beta_{coupling}}{1 + \beta_{coupling}}, \text{(undercoupled)} \tag{2.2}$$

$$|\Gamma| = \frac{\beta_{coupling} - 1}{1 + \beta_{coupling}}, \text{(overcoupled)} \tag{2.3}$$

The type of coupling is determined by the smith chart. The 1.6 cell photoinjector is overcoupled and the measured coupling beta is $\beta_{couple} = 1.7$.

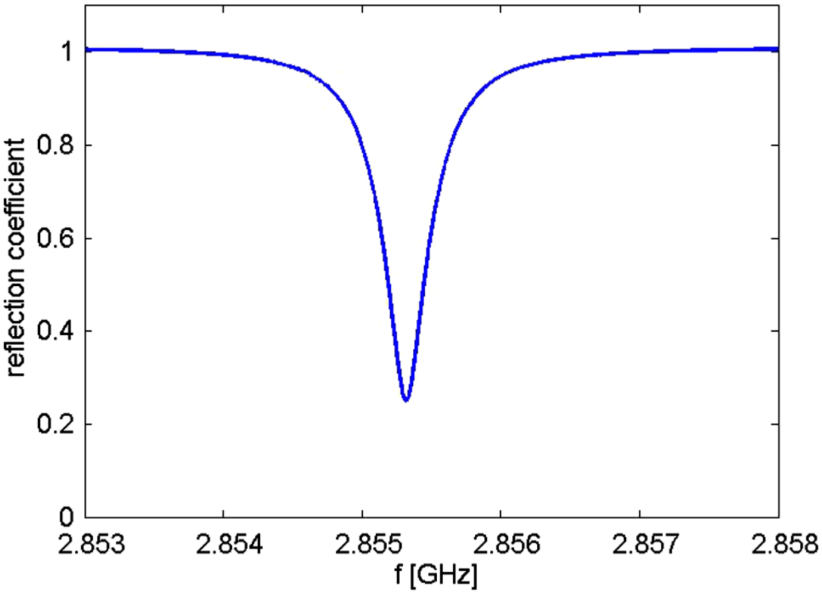

Figure 2.8: Measured resonance of the SPARC gun at 20^o

Once the structure was tuned and characterized with low RF power, we began the high power testing and conditioning process utilizing the Pegasus facility equipment mentioned in the previous section. The gun was connected to three ion pumps at 3 different locations: the input waveguide, a dipole compensating dummy hole in the full cell, and the cathode back flange. RF power was fed by the Pegasus XK5 klystron with a maximum output power of 10 MW and a maximum repetition rate of 5 Hz. The conditioning was done for approximately 5 weeks and a variable rf pulse length up to $2\mu s$. Conditioning was carried out in 8 hours period till over 50hrs of conditioning.

Conditioning consisted of measuring the power dissipated into the photoinjector using a probe as RF pulse length changes, power is increased and integrated discharges. A summary of this data can be seen for 90 hours of the conditioning in Fig. 2.9 for variation of the pulse length, gun peak power and the integrated breakdowns.

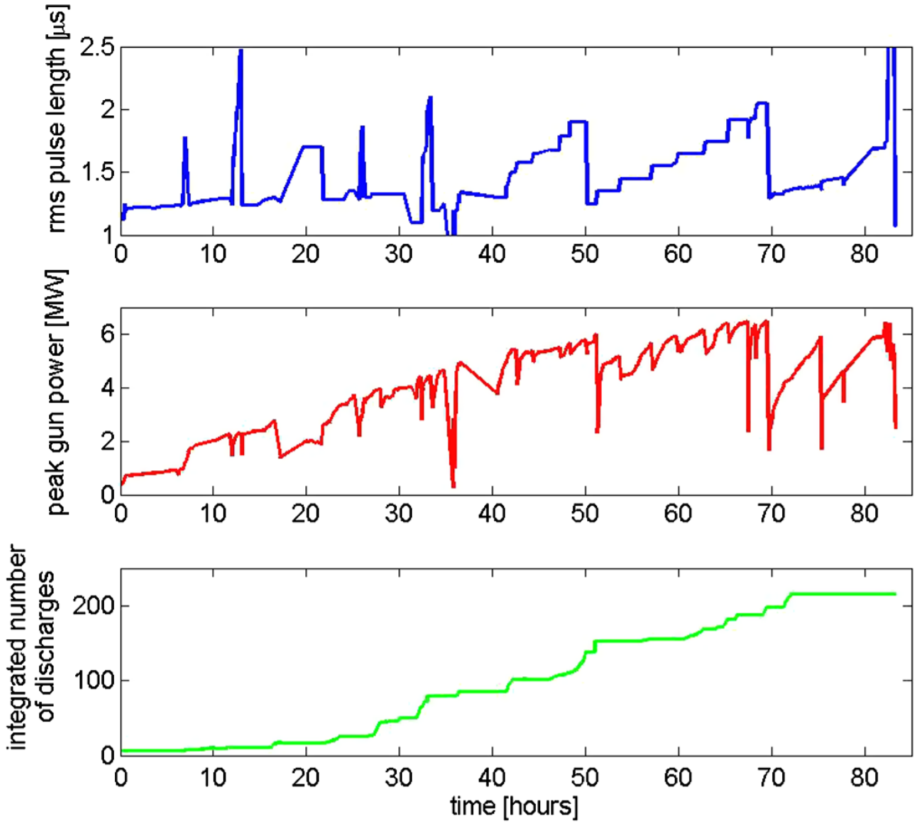

Figure 2.9: SPARC conditioning data of power dissipated into the structure as measured by the probe. (top) rms pulse length. (middle) Peak power (bottom) integrated number of discharges.

The rf signals (incident power, reflected power and transmitted power to the pickup) are monitored using the Pegasus beamline LabView control module. Samples of the incident and reflected input power are given in Fig. 2.10.

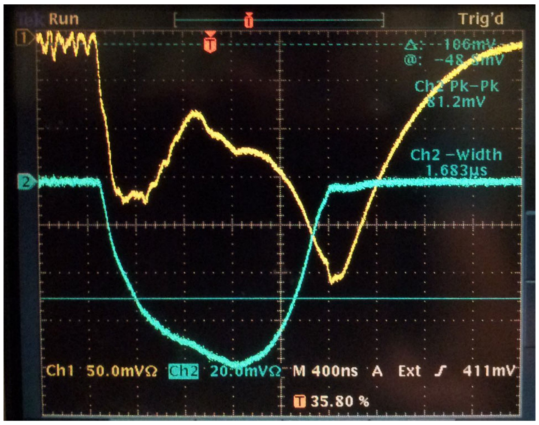

Figure 2.10: Monitoring RF breakdown during conditioning of the SPARC photoinjector during high power tests in Pegasus.

The SPARC gun was commissioned up to $10MW$ of maximum input power with an rms pulse length of $2\mu s$ which corresponded to a $92MV/m$ cathode peak field. Even though the photoinjector was designed to operate at $120MV/m$, there were limitations in the available RF power. Due to the aging of the system only up to 10 MW of peak power at a repetition rate of 5 Hz can be sent to the gun. The conditioning to higher fields was mainly limited by the available rf power. The RF breakdown rate was found to be $BDR < 5 \times 10^{-6}$ [34]. The design parameters of the SPARC 1.6 cell photoinjector have been compiled into the following reference table.

Table 2.1: Design parameters for the 1.6 cell photoinjector.

f_π	2.856MHz
Q_o	15000
Mode Separation	50MHz
Field Flatness	$< 1\%$
$\beta_{coupling}$	1.7
E_{peak}/E_{cath}	0.85
$H_{surfacepeak}$ at 120MV/m	420kA/m
Pulse Heating temperature ($2\mu s$ pulse)	$< 55°C$

2.2 1.4 cell RF photoinjector design.

In Chapter 1 we discuss the need for high brightness beams and gave an brief overview of its role in different applications. There are several approaches to increasing the beam brightness. For example, the SwissFEL experiments demonstrated a 20% reduction of the intrinsic emittance using a tunable Ti:sapphire laser source by fine-tuning the laser photon energies close to the effective work function of copper in RF photoinjectors and compensating for the QE [35]. Another method could be tailoring the emission properties of photocathodes by manipulating the surface electronic structure [36]. Ultrathin multilayered MgO/Ag(0 0 1)/MgO films have been grown using pulsed laser deposition to demonstrate an increase in quantum efficiency and simultaneous decrease in work function with layer thickness.

As shown in the Beam Brightness section of Chapter 1, the accelerating field enters all the beam brightness expressions regardless of the regime of operation. A higher extraction field has several advantages. Particles quickly accelerate away from the cathode reducing the space charge effects that limit peak brightness. Another advantage of large extraction field is allowing for very high current densities from a small area on the photocathode simultaneously reducing the initial emittance and the space-charge induced emittance growth.

Increasing the peak field involves significant redesign of the RF structures and resolving fundamental material breakdown issues. The new photoinjector focuses on increasing the beam brightness by increasing the accelerating peak electric field, E_{peak}, which is the field electrons first see when they are emitted from the photocathode.

When the electrons are first emitted, they are not relativistic yet, $\beta < 1$. For a first cell which is exactly $\lambda/2$ long, the electric field near the axis can be approximated as

$$E_z = E_0 cos(k_z z) sin(\omega t + \phi_0) \tag{2.4}$$

where ϕ_0 is the RF phase as the particle leaves the cathode surface $z = 0$ at $t = 0$, $k = 2\pi/\lambda$ with λ is the rf wavelength and $\omega = ck$. This field is produced by a sequence of RF cells in a structure operating in the π mode.

The lag associated to the low initial electron velocity creates a phase slippage between the electrons and the RF field. Once the electrons have reached relativistic speeds, they become nearly synchronous with the RF field and the slippage becomes negligible.

The slippage, ϕ_0, is written as such

$$\phi - \phi_0 = \omega t - k_z = k \int_0^z \left(\frac{\gamma}{\sqrt{\gamma^2 - 1}} - 1\right) dz \tag{2.5}$$

.

where γ is the electron's relativistic energy divided by the rest energy mc^2 with m as the electron mass.

$$\frac{d\gamma}{dz} = \frac{eE_0}{2mc^2}[sin(\phi) + sin(\phi + 2kz)] \tag{2.6}$$

.

The second term in Eq. 2.6 represents a backwards propagating wave and it is often ignored. In our case, we can omit this term because when the electrons are emitted at the cathode (z=0), we assume they carry zero kinetic energy therefore $\gamma = 1$ and the integrand in equation 2.5 is only larger than zero near the cathode region[37]. Therefore, for the region near the cathode we can rewrite Eq. 2.6 as

$$\frac{d\gamma}{dz} = \frac{eE_0}{2mc^2} sin(\phi_0) \tag{2.7}$$

.

These equations very much describe completely the rf acceleration in the cavity. It is useful to introduce the dimensionless parameter that represents the strength of the accelerating field, α.

$$\alpha = \frac{eE_0}{2mc^2k} \tag{2.8}$$

.

With this parameter we can write an approximation for the particle energy

$$\tilde{\gamma} = 1 + 2\alpha sin(\phi_0)kz \tag{2.9}$$

.

Solving the integral in equation 2.5 with these approximations, we get

$$\phi - \phi_0 = \frac{1}{2\alpha sin\phi_0}[\sqrt{\tilde{\gamma}^2 - 1} - (\tilde{\gamma} - 1)] \tag{2.10}$$

.

The equation 2.10 shows a dependence not only on E_0 but also the initial launch phase.

The electrons are very quickly accelerated away from the cathode. Once the electrons have reached relativistic speeds, they become nearly synchronous with the RF field and the slippage becomes negligible and the phase approaches an asymptotic value so the integrand in 2.5 is only relevant near the cathode. The asymptotic phase, ϕ_∞, is written as

$$\phi_\infty = \frac{1}{2\alpha sin(\phi_0)} + \phi_0 \tag{2.11}$$

.

Kim shows that also for transverse beam dynamics reasons the asymptotic phase for maximum energy at beam exit should be $\pi/2$[37].

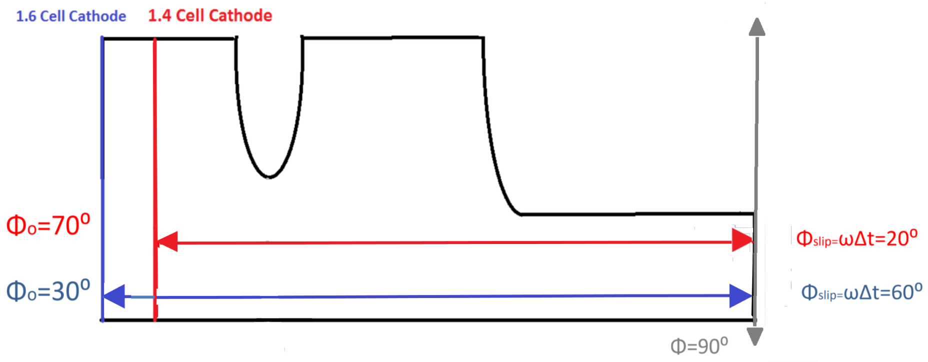

Figure 2.11: Shortening cathode cell for slippage reduction

Typical 1.6 photoinjectors have an optimal launching phase of $25^\circ - 35^\circ$ depending on the input RF power. The 1.4 cell photoinjector was found to have an optimal launching phase of 70° in simulations which it is close to the predicted phase. The higher launching phase increased the extraction field compared to the 1.6 cell photoinjector by a factor of $\sin(70^\circ)/\sin(30^\circ) = 1.9$. This simple method increases the beam brightness by at least a factor of 1.9 and even higher depending on application and operation regime.

To increase the launching phase and reduce the slippage, we have chosen to shorten the cathode cell from the typical to 0.4λ cell photoinjector as shown in Fig. 2.11.

2.2.1 Cathode cell length

Historically, the 0.6λ cathode cell length has risen from the evolution of photoinjector design driven by applications for very high charge (nC) beams such as linear collider or first generation FEL designs. The longer first cell was beneficial due to the higher gun output energy and improved focusing characteristics. First photoinjector designs were using a 0.5λ (half-cell) to house the photocathode. These include structures such as the LANL 1.3 GHz (L-band) gun with 5-cells [38]. This electron gun was built when photoinjector technology was new and had design issues such as poor emittance compensation and unbalanced fields from cell to cell. The gun operated at 0.1% duty factor requiring 2.4 MW of RF power to produce a 0.6 MW beam. Another structure was the DESY Zeuthen (PITZ) 1.5 cell L-band cavity with coaxial rf coupler in 2002 [39]. Most structures in the early years were designed to work with bunch charges in the nanoCoulomb scale, typically simulation design was done for 1nC.

The appropriate cathode cell length is usually chosen during design optimization to fit the needs of the application and capabilities of the rest of the system. A recent study for electron gun of 1.4, 1.45, 1.5, 1.55 and 1.6 cell geometries was conducted to see the optimal cathode cell length in various experimental set-ups [[20]]. Simulations for each structure was done for 10pC, 100pC and 1nC bunch charges.

In our case, it is useful to focus on the 1.6 and 1.4 cell geometries. In fig. 2.12 shows the results for a bunch charge of 10pC. This plot shows the horizontal emittance of the two structures and find a lower emittance in the 1.4 cell geometry and 20% increase in brightness for the 1.4 cell case relative to the 1.6 cell case[20].

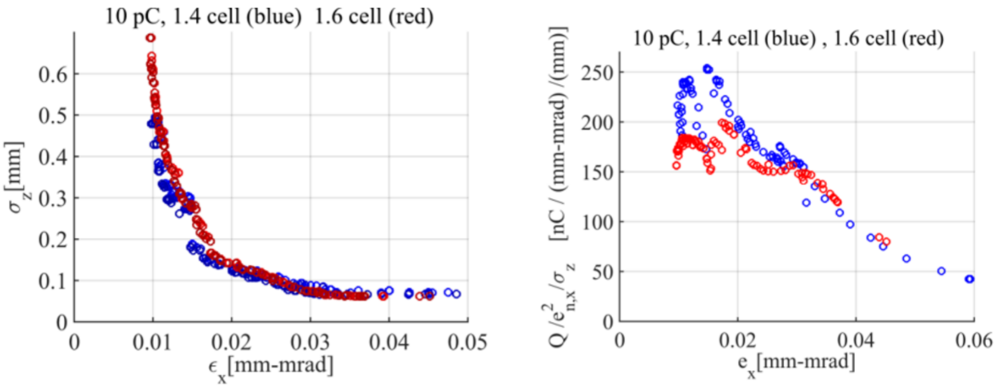

Figure 2.12: (left) The optimal horizontal emittance and rms bunch length for 10pC for 1.4 and 1.6 cell geometries. (right) Brightness vs. transverse emittance. Courtesy figure from Alex Cahill

In the case of 1nC bunch charges, which most older generation of RF photoinjectors used, the 1.6 cell electron gun outperforms the 1.4 cell gun. The 1.6 cell geometry has a higher peak beam brightness than the 1.4 cell gun as shown in figure 2.13.

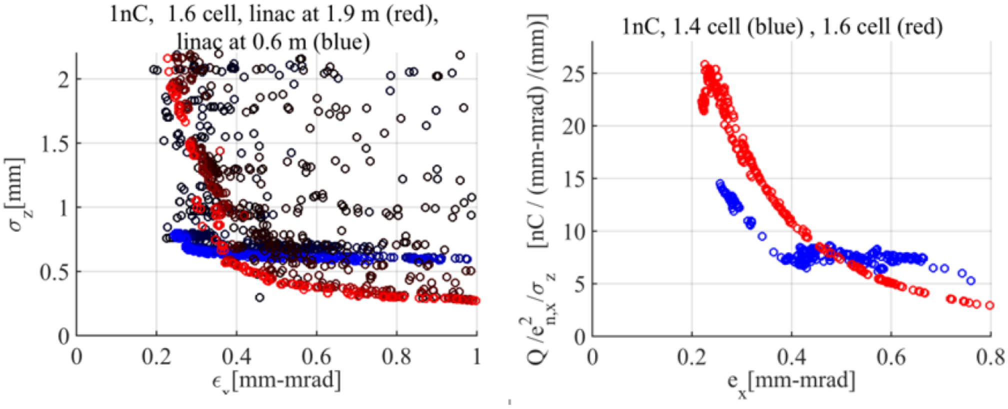

(a) (b)

Figure 2.13: (left) The optimal horizontal emittance and rms bunch length for 1nC for 1.4 and 1.6 cell geometries. (right) Brightness vs. transverse emittance. Courtesy figure from Alex Cahill

The 1.6 cell gun has been the go-to geometry to handle large bunch charges. In our case, we aim to use pC bunch charges and the 1.4 cell geometry is the preferred choice.

2.3 Beam Dynamics

The beam dynamics have been studied using General Particle Tracer (GPT) code. The field maps used in GPT were extracted from the HFSS code for a 120MV/m peak electric field. In Fig. 2.14, the energy dependence on the injection phase for the 1.6 and the 1.4 cell structure can be seen with 120MV/m peak electric field. The optimal phase is the one for which the maximum output energy is achieved. The reduction of the accelerating region on the 1.4 cell photoinjector causes the output energy to be

10 % lower than the SPARC photoinjector but the final electron beam energy is not a critical parameter for any of the main applications of high brightness beams. as long as particles are fully relativistic and, breakdown permitting, in principle it could be compensated by a slightly higher peak field. A 1D field analysis has been included in the beam brightness study. One of the characteristic of these type of cavities is the on-axis field profile. Cylindrical symmetry allows the EM field components near the axis to be approximated by a power series in the radial coordinate. These power series are substituted into Maxwell's equations and therefore all field components can be determined by simply knowing the on-axis field profile.

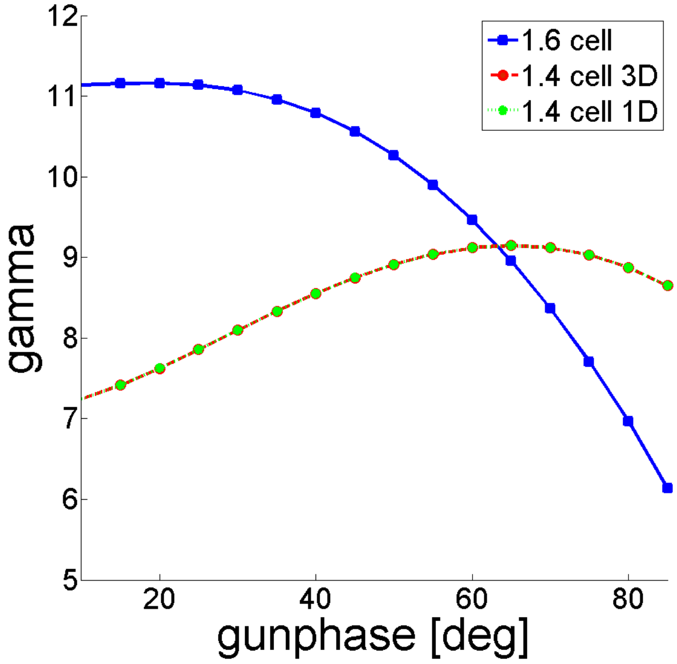

Figure 2.14: Gamma vs. injection phase at 120MV/m peak electric field.

At the gun exit, there's typically an emittance compensation solenoid acting as a lens which aids with steering and focusing the beam. The beam energy spread can introduce additional emittance in the solenoid due to different electrons longitudinal slices in the beam having different focal lengths. The energy spread as a function of injection phase is also shown in Fig. 2.15. For the 1.4 cell design the minimum energy spread is obtained at $65 - 70^\circ$ in correspondence to the maximum energy point as expected.

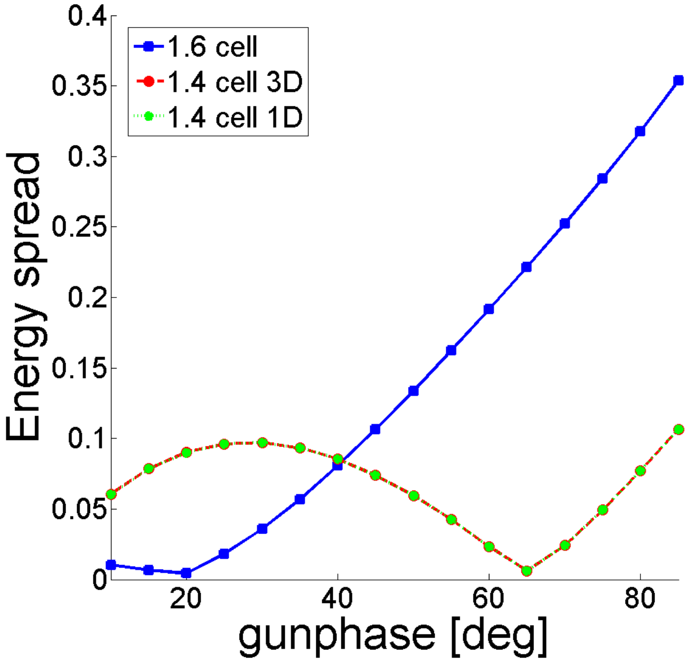

Figure 2.15: Relative energy spread vs. phase for SPARC 1.6 cell(blue),1D MATLAB analysis for the 1.4 cell (red) and 3D GPT simulation for the 1.4 cell (green) at 120MV/m peak electric field.

The different electric field profile has important consequences on the longitudinal phase space dynamics. In particular the 1.4 cell gun profile can impart a much stronger negative position-energy correlation on the beam. It is useful to look at the compression ratio, the ratio between the the electron bunch length at the gun exit and the initial laser pulse length, as a function of injection phase (Fig. 2.16.

Compression of the bunch has been observed when the trailing end of the bunch is emitted an RF phase causing a larger accelerating gradient than the front of the bunch is experiencing [40]. Usually, space-charge forces, which stretch the bunch, will counteract the compression. Both of these effects are more significant near the cathode region before the bunch becomes relativistic.

The bunch compression can be calculated by taking the derivative of the asymptotic phase with respect to the initial phase such as

$$\frac{\Delta\phi_\infty}{\Delta\phi_0} = 1 - \frac{cos(\phi_0)}{2\alpha sin^2(\phi_0)} \tag{2.12}$$

This quantity is calculated for very low beam charge so that it is possible to neglect space charge effects[17]. For 120 MV/m peak fields and similar injection phases the compression ratio is about twice as large for the 1.4 cell gun than the conventional 1.6 cell design.

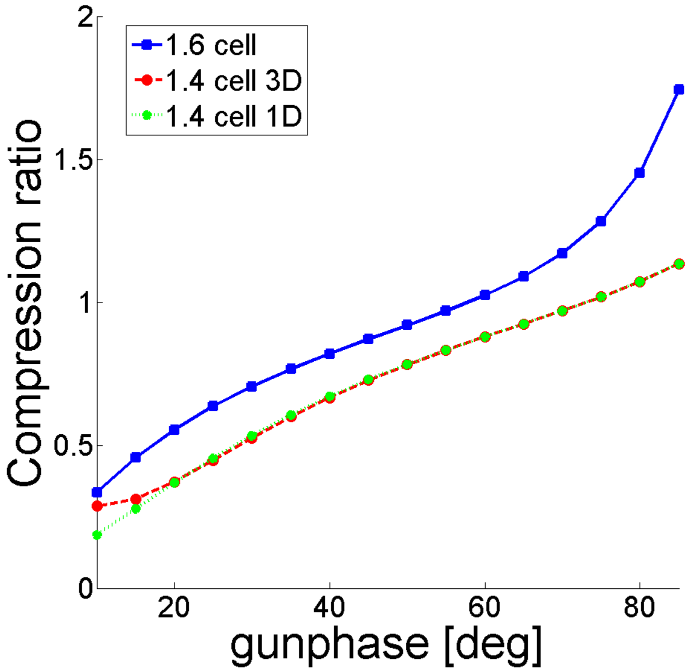

Figure 2.16: Compression ratio vs. phase for SPARC 1.6 cell(blue),1D MATLAB analysis for the 1.4 cell (red) and 3D GPT simulation for the 1.4 cell (green) at 120MV/m peak electric field.

2.4 Electromagnetic Design

The 1.4 cell RF photoinjector electromagnetic design has been done using the SUPERFISH, HFSS by Ansys and General Particle Tracer (GPT) simulation codes[41][42][43]. In this section, we will discuss the optimization of the launch phase for higher beam brightness and the photoinjector rf and electromagnetic design in 2D and 3D.

2.4.1 2D electromagnetic design

SUPERFISH was used for the 2-D design. The first RF design task done is SUPERFISH is to construct the generic geometry, meaning that it excludes any asymmetries or ports. The main parameters determined in this step is the cell radia.

A simple MATLAB code was written to generate the contour coordinates of the 2D profile of the gun starting from a basic 1.6 cell electron gun for 2.856GHz with a square shaped iris [44]. The code feeds the geometry for SUPERFISH to analyze and records the resonance frequency upon completion. If the resonance frequency is not as desired, MATLAB will automatically arrange the contour geometry with the boundaries and steps specified and re-starts the process. This process is the automated until the contour yield the desired frequency, in our case 2.856GHz.

This frequency tuning assumes a lossless cavity but it is a good starting point for figuring out the range in which the cell parameters yield the correct frequency in the π mode. The 2-D profile of the cavity is shown in 2.17.

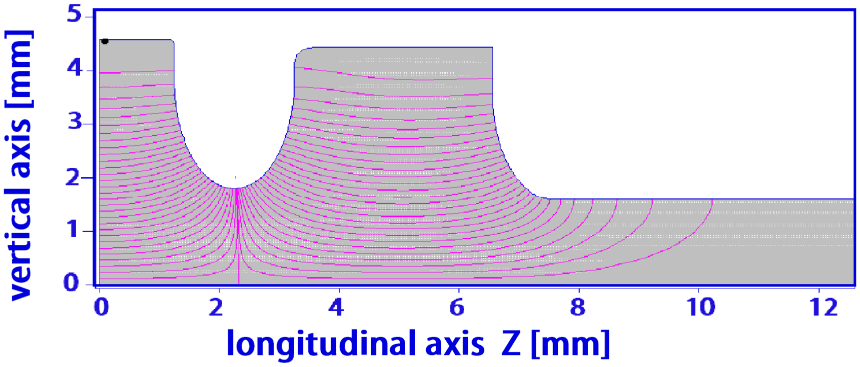

Figure 2.17: 2D map of the π mode in a 1.4 cell electron gun in SUPERFISH.

The next optimization step is to balance the field. The goal is to achieve peak fields in each of the cells with the same magnitude. At this point, the cell radia have fluctuate around the preliminary frequency parameter found until the electric field longitudinal profile is balance across the structure.

The balanced longitudinal electric field on axis is shown in 2.18.

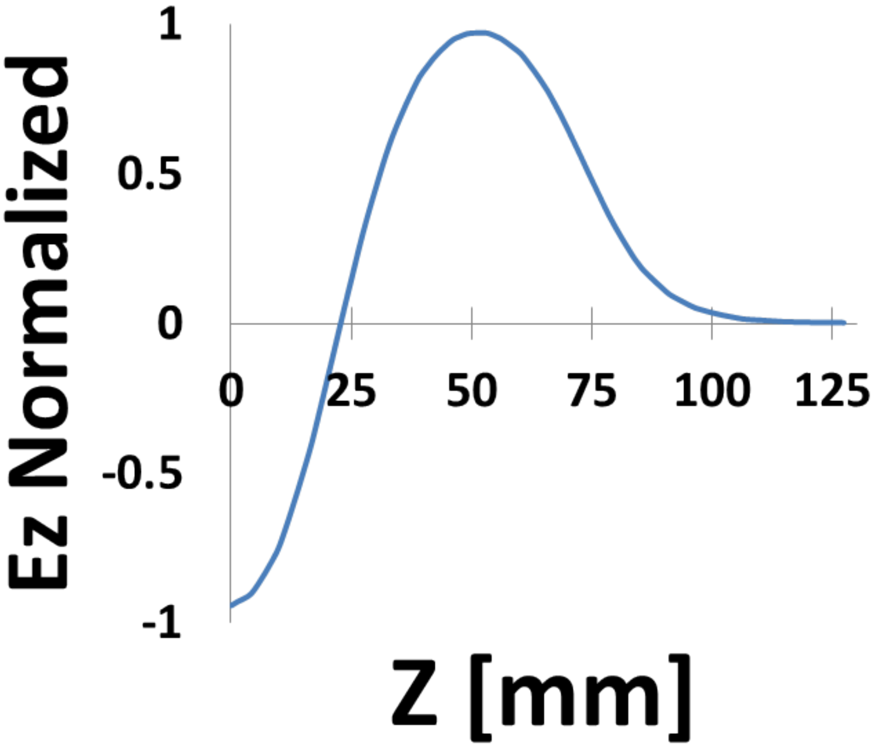

Figure 2.18: Normalized longitudinal electric field on axis in SUPERFISH

The third step of the 2D optimization is to tailor the iris geometry. The iris is a key feature in the design of electron guns and often pose difficult fabrication techniques. The iris couples the cathode cell and the full cell. In this step, we avoid any high concentration of field lines but most importantly, we aim to have the surface peak field at the cathode higher than the peak field at the iris.

There are two unique features in the particular iris we ended up choosing for our project. First, the iris diameter has been increased to $2r_{pipe} = 36mm$ where as the previous versions of existing 1.6 cell RF guns have an iris diameter of 20mm or less.

The main benefit of increasing the iris diameter is the frequency separation it creates between the 0 and π mode. This mode separation prevents the modes from overlapping and negatively impacting the beam dynamics. Further discussion of mode separation will be included in the 3D optimization of the gun design. Another advantage of the larger iris diameter is increase in pumping speed in the cathode cell.

The second feature of the iris is the elliptical shape with an iris ratio of b/a. The strong rounding reduces the field at iris. Ideally, the field at the iris should be lower or comparable to the field at the cathode. The normalized surface electric field profile is shown below in fig. 2.19. .

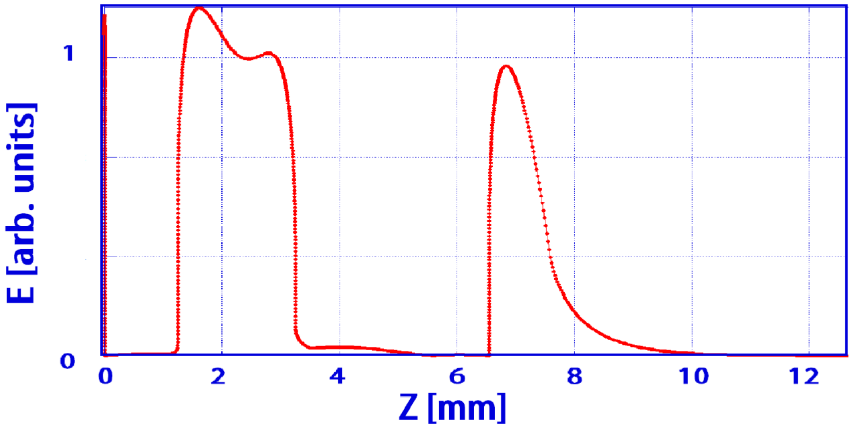

Figure 2.19: 2D surface field map.

In Fig. 2.19, we see the electric field at the iris is only 5% larger than the field at the cathode. Ideally, the maximum of the electric field in the photoinjector should occur at the cathode.

2.4.2 3D electromagnetic design

The rest of the design was finalized using the 3D electromagnetic code HFSS by Ansys.The 3D design now must include all the ports and asymmetries in the structure. The 1.4 cell photoinjector has the features shown in Fig 2.20. The 1.4 cell gun includes a chamfered cathode cell with 2 laser ports at oblique angles with respect to the cathode. It includes strongly rounded iris coupling the cathode cell and the full cell. It also features a full cell shape that is not cylindrically symmetric with flat walls at the coupling port and pumping port and the beam exit pipe.

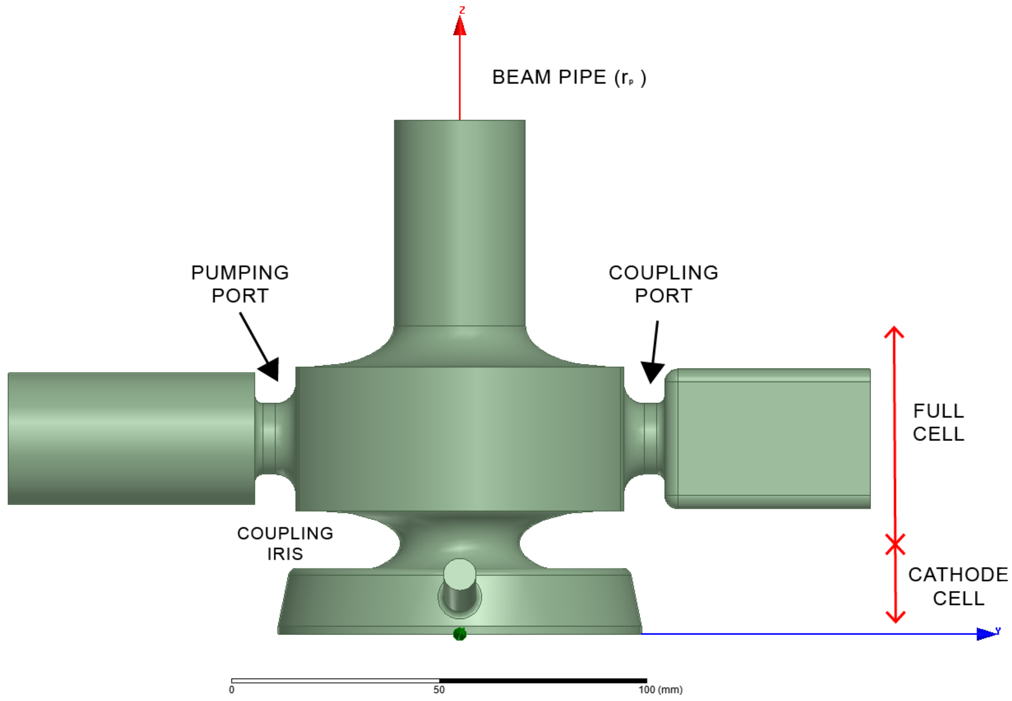

Figure 2.20: 1.4 cell photoinjector's cavity main components

2.4.2.1 Power Coupling

The two main types of power coupling are via a waveguide or a coaxial type coupling. Standing wave (SW) cavities can be coupled using slots on waveguides or loops in coaxial couplers. Each method has advantages and drawbacks and generally calculating the power transfer is not trivial and 3D simulations are often the only way[45].

Coupling slots not only change the geometry of the structure but the geometry of the waveguide as well. Each slot offers a power transmission opening where power can flow in and out of the cavity. Waveguide coupling can handle large power loads. Even though the large size of the coupling slots can be considered a drawback, it also allows easier cooling and faster pumping speed. The biggest drawback of waveguide coupling is that it is fixed and any variations are difficult to achieve once the part is fabricated.

Analytical solutions to this power transfer are difficult. If the slot is small enough, perturbation theory can be used and we can model the slot as a small magnetic dipole with a dipole moment proportional to the magnetic field tangent to the surface of the port, $H_{||}$. This magnetic dipole introduces a field into the structure which distorts the desired EM design desired. Coaxial couplers often can be modeled using a loop model. The loop has more or less the same effect as the slot coupling. It acts as a dipole and introduces a magnetic field into the structure. Perturbation theory is also used if the loop is sufficiently small [33].

Coaxial couplers can also utilize an antenna. In this case, the inner conductor of the coaxial is inserted into the structure. A surface electric current then flows on the surface and the antenna acts as an electric dipole with a dipole moment proportional to the current density perpendicular to the inner conductor surface.

Coaxial couplings uses more complex designs. The advantage of this method is the fact that the emittance compensation solenoid can be moved much closer to the cathode as it is not impeded by the presence of the waveguide[45].

The power coupling method chosen for the 1.4 cell gun was a waveguide slot located on the side-wall of the full cell as shown in the schematic above, Fig. 2.20. The port profile is a strongly rounded racetrack geometry. The dimensions of the port are tailored to be able to use short pulses (large coupling beta factor) while minimizing the pulse heating temperature rise. The strongly rounded edges prevents large concentrations of surface magnetic fields and therefore reduces the pulse heating and consequently breakdown probability rate as seen in equation 1.5. The surface magnetic field on the port is shown in 2.21.

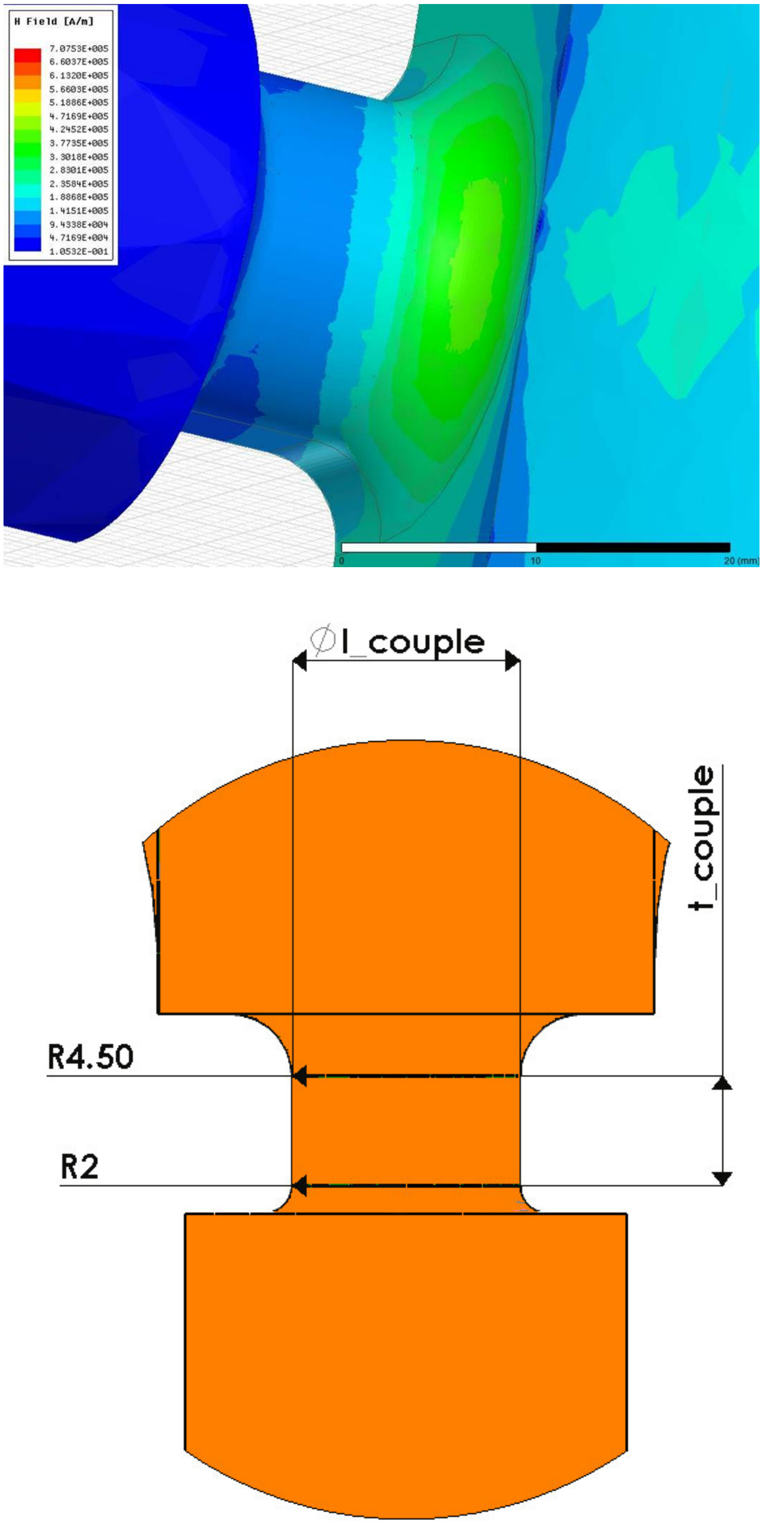

Figure 2.21: (Top)Surface magnetic field of the coupling port on HFSS for 120MV/m gradient.(Bottom) Coupling port schematic.

The maximum allowed surface magnetic field was calculated to maintain the pulsed heating temperature rise $\Delta T < 60^o C$ with a gradient of 120MV/m using a square pulse of $2\mu s$. The maximum surface field allowed corresponds to 480kA/m.

In the introduction we discussed the $\beta_{coupling}$ parameter. This coupling coefficient has been increased to 1.98 for an overcoupled scheme. The increase in the coupling beta lowers the loaded quality factor, Q_L. This is accompanied with a shorter filling time which allows reaching the same cathode peak field while using shorter pulses albeit of higher peak power. While using shorter pulses is an advantage, the separation between the 0 and the π mode must be increased to avoid exciting the 0 mode in the transient. The mode separation achieved is $30MHz$ with the 0-mode at $2.826GHz$, which is twice as large as the mode separation found in older versions of the S-band high gradient photoinjectors.

A consequence of exciting both the 0 and the π modes is seen in the emittance and energy spread. When the 0-mode is excited is causes a unbalance in the fields, meaning the peak field in each cell is no longer has the same magnitude. This unbalance produces a correlated energy along the bunch.

Every port or asymmetry introduced in the structure changes the fields in the structure and require corrections. As mentioned above, the coupling slot introduces asymmetries in the field distribution. These effects create the maximum accelerating field to not be located in the beam line axis but rather towards the port opening. This could have a negative affect on the beam. For a relativistic beam in a cavity in the TM mode we can write the traverse momentum imparted by the rf fields as [46],

$$p_{\perp} = \frac{e}{v} \int_0^{L_{cav}} [\vec{E}_{\perp} + (\vec{v} \times \vec{B})_{\perp}] dl \tag{2.13}$$

where $\vec{E}$ and $\vec{B}$ are the electric and magnetic field and dl the direction of the beam, typically directed along the z-axis. Using standard definitions and vector identities, we can re-write it in terms of the vector potential.

$$p_x = -\frac{e}{v}\int_0^{L_{cav}} \left\{\frac{d\vec{A}}{dt} - [\nabla(\vec{v}\cdot\vec{B})]\right\}_x dz \tag{2.14}$$

Assuming constant velocity, v, equation (2.15) reduces to

$$p_x = -e\int_0^{L_{cav}} \left\{\nabla A_z]\right\}_x dz \tag{2.15}$$

Since the z-component of the vector component assumes the form $A_z = A_0 e^{i\omega t}$, there's a time-dependent dipole kick [47]. Eq. 2.15 is another form of the so called Panofsky Wenzel theorem which relates the longitudinal fields in the structure to the transverse impulse.

We can write the magnetic field near the beam axis as

$$B_\phi(r,\phi,z) \cong A_0(z)r + \sum_{n=1}^{\infty} A_n(z)cos(n\phi)r^{n-1} \tag{2.16}$$

where A_n usually are complex and z-dependent component. A_1 is the dipole component and A_2 is the quadrupole component, etc... The most common method to reducing the dipole field corresponds to reducing the amplitude A_1. This can be achieved by creating an identical port directly across the coupling port. This second port regenerates symmetry in the fields near the axis and nearly cancel all dipole effects. There will always remain some dipole moment effects as the RF power is still being fed by a single feed. Dual-feeds can be used for full compensation. This method generally uses a power splitter into two lines but it introduces a higher level of complexity in the power distribution system.

2.4.2.2 Magnetic moments compensation.

As mention above, a magnetic dipole is introduced with the waveguide coupling method we've chosen. Our approach to compensate for this field disturbance is by introducing a second port symmetric to the waveguide coupling port. The dipole compensation port will serve as the main the pumping port. This port also offers the advantage of increasing the pumping speed.

It is also important to correct for the rest of the moments that have a significant impact on the fields near the axis. The quadrupole moment, A_2, has a smaller effect on the beam dynamics but still significant enough to be seen and worth correcting. The magnitude of the quadrupole moment near the axis can be estimated by looking at the variation of the magnetic field around the z-axis such as

$$A_2(z) = \frac{B_{max}(r_0, z) - B_{min}(r_0, z)}{2r_o} \tag{2.17}$$

where r_0 is the distance to the z-axis.

In order to compensate the quadrupole moment a choice was made so that the full cell of the 1.4 cell cavity does not posses cylindrical symmetry. The cross section of the full cell is the intersection of 2 circles with their centers located at an offset,Δy, from the gun z axis. Two flat planes truncate the cell where the circles meet as shown in Fig. 2.22.

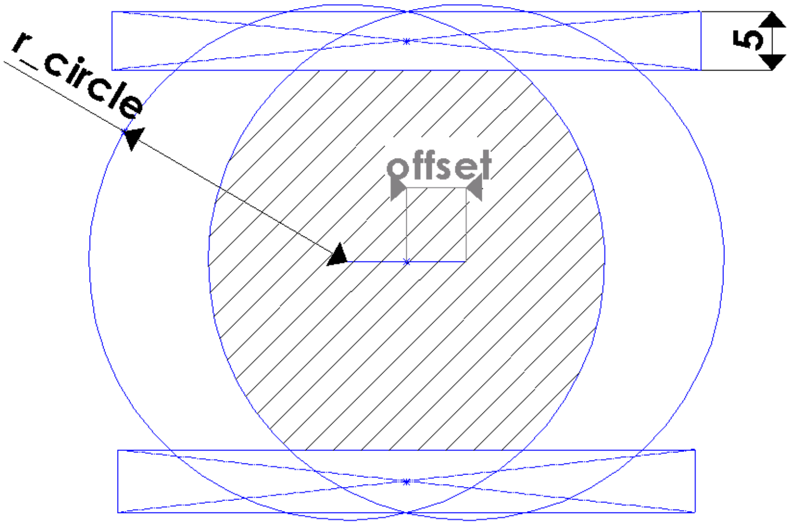

Figure 2.22: Full cell cross section geometry

The measurement estimate of the quadrupole moment was performed using simulation data along 4 circles of different radii (2mm, 3mm, 4mm and 5mm) located at the center of the full cell as shown in fig. 2.23. In the figure 2.24, we show HFSS simulation results for the magnetic field along each of these loops. As we can see in equation (2.4.2.2), it is desired to have a constant magnetic field along each loop as the quadrupole moment depends on the variation of the magnetic field. The field flatness on each of these loops indicates the reduction of the quadrupole moment in the full cell.

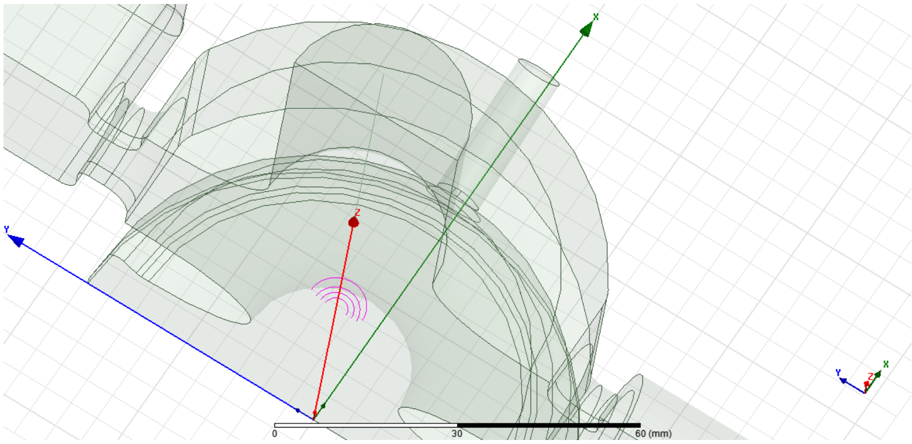

Figure 2.23: Geometry used to measure the quadrupole moment. Four circles around the z-axis and centered on the full cell. Radii of 2mm, 3mm, 4mm and 5mm.

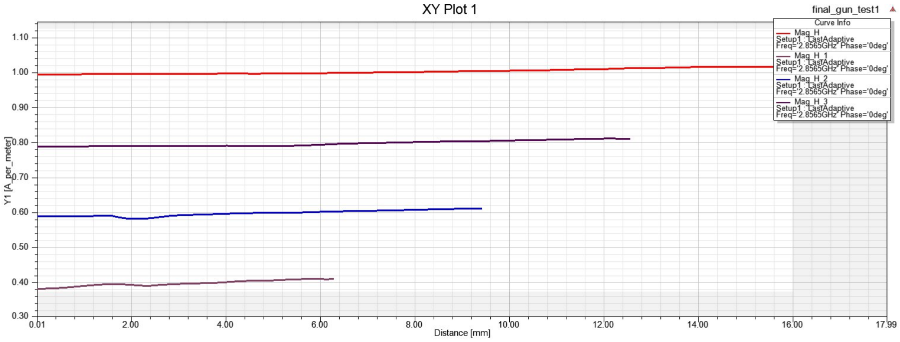

Figure 2.24: The magnetic field magnitude measure along circles centered in the full cell measuring the quadrupole moment for circles of radii 2mm, 3mm, 4, and 5mm centered on the z-axis.

To further understand and appreciate the improvements in the quadrupole moment compensation, we repeated simulation to compare it with the SPARC 1.6 photoinjector. In Fig. 2.25, we show the magnetic field fluctuations along a circle of 2mm around the z-axis and centered in the full cell. From this plot we see the difference between the 1.6 cell, which has an un-corrected quadrupole moment, and the corrected 1.4 cell gun.

In Fig. 2.25, we can see no fluctuation in the magnetic field around the axis of the 1.4 cell photoinjector compared to the 1.6 gun. Therefore, the full cell geometry has compensated for quadrupole kick of the gun.

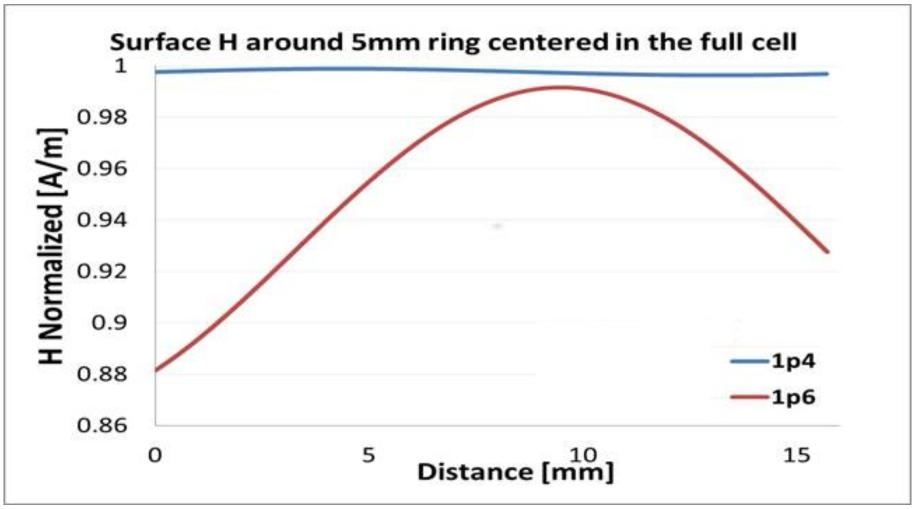

Figure 2.25: Normalized magnetic field along a the 2mm ring around the z- axis at the center of the full cell.

2.4.3 Summary of design parameter

A summary of the 1.4 cell rf photoinjector design parameters discussed in this chapter can be found in the following table.

Table 2.2: Design parameters for the 1.4 cell photoinjector.

f_π	2.856MHz
Q_o	13411
Mode Separation	30MHz
Field Flatness	$< 1\%$
$\beta_{coupling}$	1.98
$\lvert\Gamma\rvert$	0.331
E_{peak}/E_{cath}	1.05
$H_{surfacepeak}$ at 120MV/m	480kA/m
E_{max} for $P_{in} = 1W$	24,300V/m
Pulse Heating temperature ($2\mu s$ pulse)	$< 60°C$

2.5 Photocathode components

The photocathode is a very important component of RF photoinjectors and their design. The selected cathode needs to be capable of providing an electron beam with the necessary parameters that the experiment demands. Until now we have concentrated in the design of the radiofrequency resonant cavity tailoring the electromagnetic fields in the structure that the electron beam will experience after emission. In this section, we will discuss the feature of the UCLA 1.4 cell photoinjector that involve the photocathode. It is useful to review few aspects related to the development of photocathodes for electron sources, the physics of cathodes, the photo-emission process, recent advances in cathode research ,and how the UCLA photoinjector will play a role in this area of research.

2.5.1 Basics of photocathode emission

Albert Einstein won a Nobel Prize in 1921 for the first theory that described the process of photo-emission, the photoelectric effect [48]. The photoelectric effect is the observed phenomena of electrons being emitted from a bulk material when incident light of specific wavelength ranges is shined upon the surface of the material. This theory proposed the idea that in order for photoemission to occur photons, the quantization of the energy of light, must possess an energy larger than the material the work function, ϕ_{eff}, which is the potential electron must overcome in order to escape the material. The photoelectric effect is described as a three step model: photon absorption, electron transport and emission. A more detailed derivation of the topic in the context of high brightness electron sources can be found in the article "Quantum efficiency and thermal emittance of metal photocathodes" by D. Dowell [49].

The three step model makes two main assumptions. The first is that on the initial electron distribution in the material. For exposition purposes we can assume a conductor at zero temperature, even though this can be modeled more precisely in refinements of the theory [50] the material is treated as a conductor a. The second is that every photon absorbed excites an electron. Since no selection rules are needed, this simplifies the model to explain indirect transitions where energy is conserved but the electron's transverse momentum is not. This model is particularly good for metal photocathodes.

The first step begins with incident laser light on the material. The relationship between transmission $T(\nu)$ and reflection $R(\nu)$ probability is written as

$$T(\nu) = 1 - R(\nu) \tag{2.18}$$

How far the photon will travel into the material will depend on the absorption coefficient of the medium. The probability of exciting an electron depends only on the electronic density of states. The fraction of the electron excited to a higher level is expressed as the probability of excitation divided by the total number of transitions and it is written as

$$P(E, h\nu) = \frac{N(E)N(E - h\nu)}{\int_{E_f}^{E-f+h\nu} dE' N(E')N(E' - h\nu)} \tag{2.19}$$

where $N(E - h\nu)$ is the number of initial states, $N(E)$ is the final number of final states. The denominator in 2.5.1 is the total number of transitions where the lower integration limit rises from the Pauli exclusion principle since all the levels below the Fermi energy level are occupied.

The second step of the model tackle the probability of the electron reaching the surface of the metallic photocathodes. Even though the first step is the same with conductors and semi-conductors, in the second step they are treated very differently. We will focus for now on the metallic case (a.g. copper cathodes). The main process that dominated step two is scattering. The largest contribution to the scattering is the e-e interaction. Other scattering events such as ones due to impurities or phonons are ignored in this treatment.

The photon absorption length is λ_{ph} and from this depth the electron will travel towards the surface of the metal cathode. The length an electron can travel inside the bulk is λ_e which is limited by the scattering events. The fraction of electrons that successfully will reach the surface can be written as

$$T(E,\nu) = \frac{\lambda_e/\lambda_{ph}(\nu)}{1+\lambda_e/\lambda_{ph}(\nu)} \tag{2.20}$$

.

The third step involves the electron escaping the metal surface. The material has a work function, ϕ_w that is determined by the material. The work function is the minimum energy an electron must have in order to escape in absence of an external electric field.

In our case, there is an external electric field on the cathode so the work function has to be modified. This is known as the Schottky effect. The effective work function of the metal surface can be written as

$$\phi_{eff} = \phi_w - \phi_{Schottky} \tag{2.21}$$

.

where $\phi_{Schottky} = e\sqrt{\frac{eE_0}{4\pi\epsilon_0}}$ is the work the external field adds to the process.

An schematic of the three step model is shown in fig. 2.26 to illustrate these processes [49].

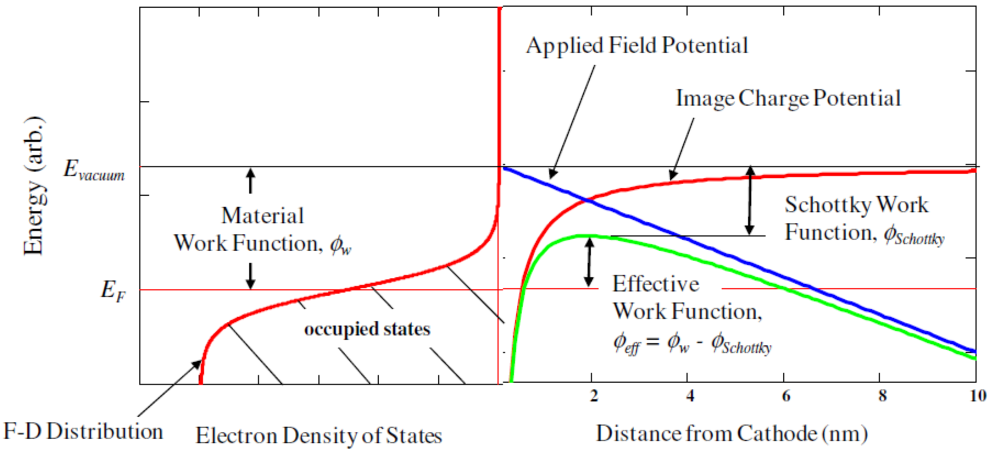

Figure 2.26: Stages of three step model of photoemission for metal cathodes under an external electric field. Re-printed from reference above by Dowell, 2009.

2.5.1.1 Figures of merit

There are multiple features that we look for when choosing a cathode but nearly all parameters are determined by the cathode material and the laser. There are two important terms used to characterize photocathode, The first one is the quantum efficiency (QE). We define is as

$$QE = \frac{n_e}{n_p} = \frac{h\nu}{E_{laser}}\frac{q}{\epsilon_0} \tag{2.22}$$

where n_e is the number of emitted electrons, n_p is the number of the incident photons, $h\nu$ is the photon energy measured in electron volts, eV, E_{laser} is the energy of the laser measure in joules and q is the electron charge measured in Coulombs.

The second useful quantity is the intrinsic emittance (IE). The distribution of intrinsic transverse momentum of the electrons in the cathode is a characteristic of the material of choice, the incident laser energy and the extraction field. This emittance is usually calculated by looking at the variance of momentum of the electrons at emission. IE can be described as

$$\epsilon_n = \sigma_x \sqrt{\frac{h\nu - \phi_{eff}}{3mc^2}} \tag{2.23}$$

A related quantity is the mean transverse energy spread (MTE) which measures the electron temperature at emission [22]. The MTE depends on the cathode material and drive laser wavelength [49]. These few parameters are fundamental limiting factors in the acceleration of the electrons.

Copper cathodes have been a reliable cathode solution for many years. Cu cathodes are cheap, easy to to manufacture, durable and work well in a range of vacuum pressures. Copper photocathodes generally work at a wavelength range of 250-270nm. They have very high MTE (500MeV) and very low QE(10^{-5}) at the usual emission wavelengths [51]. A copper cathode will be the base option for the new 1.4 cell gun. We will discuss below the possibility of using other cathode materials.

2.5.2 Laser ports

Recently, it has been demonstrated that a very small drive laser spot size on the cathode generates ultra-low emittance beams using the SPARC 1.6 cell photoinjector at UCLA. The 1.6 gun has 2 laser ports at 72° with respect to the beam axis, as shown in 2.5.2. This angle allows the laser to illuminate the cathode at an oblique incidence with a tightly focused ultrafast (100fs) laser pulse on the cathode.[52]

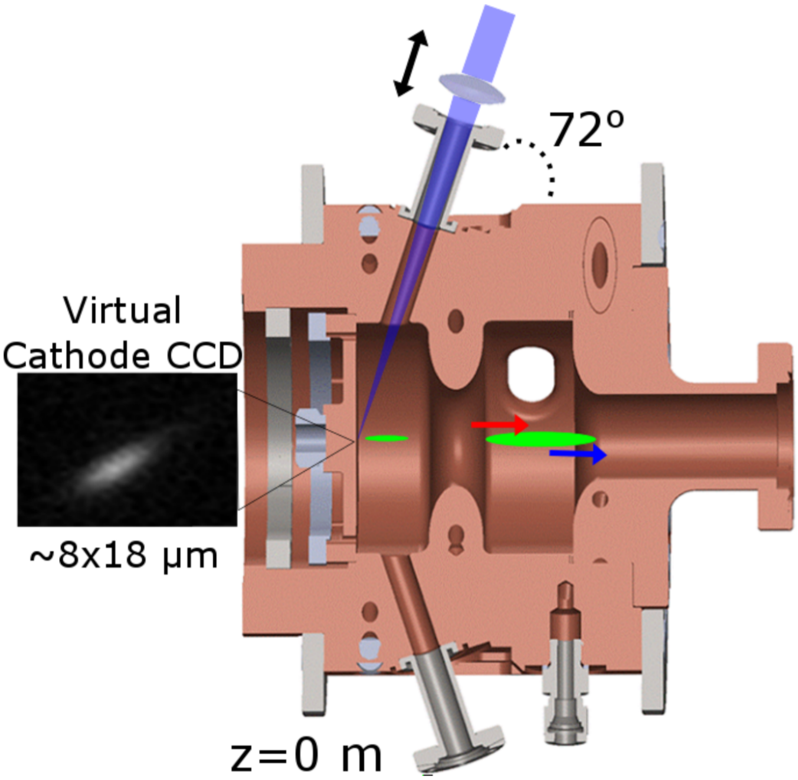

Ultralow emittance (20 nm, normalized) electron beams with 105 electrons per bunch are obtained by tightly focusing an ultrafast (100 fs) laser pulse on the cathode of a 1.6 cell radiofrequency photoinjector.

Using the oblique incidence allowed reaching emittance as low as 5nm-rad at 20fC. Results are shown in fig. 2.27.

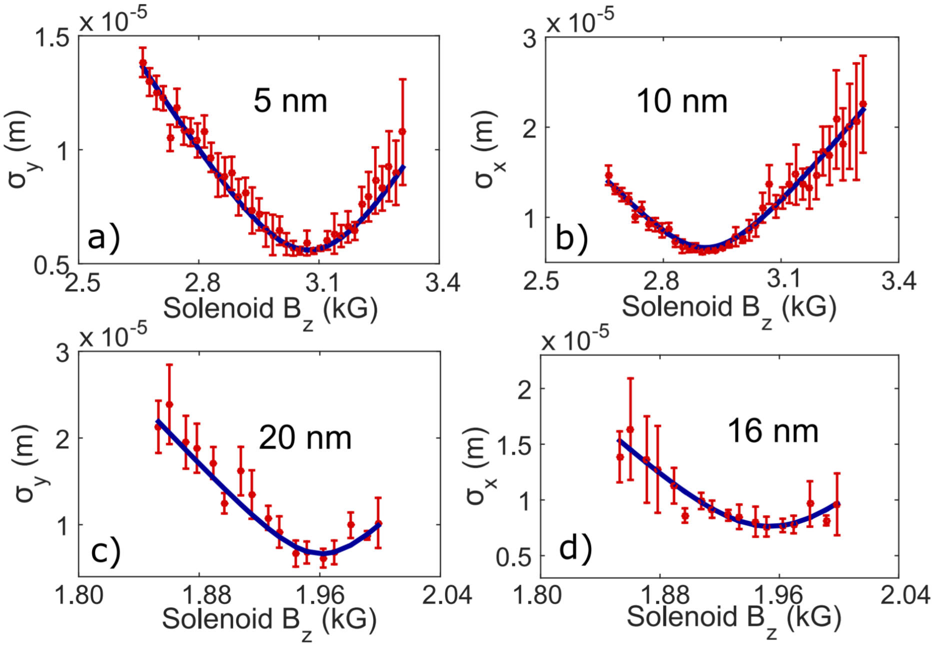

Figure 2.27: Normalized transverse emittances in y. (a) and x (b) for a $\sigma_{t,uv} = 1.1 ps$ laser pulse on the photocathode, accelerated on crest in the Pegasus Linac. c) and d) show normalized emittances for a $\sigma_{t,uv} = 100 fs$, in the velocity bunching configuration

In these experiments, the laser pulse was long at the cathode and was later compressed by the use of a radiofrequency cavity reaching the 7 fs rms value. Crossing the 10fs threshold in electron bunch length can enable breakthrough opportunities for compact electron sources, with applications ranging from ultrafast electron diffraction and microscopy amongst others. Therefore, the laser ports of the 1.4 cell photoinjector were designed to continue to allow on the oblique incidence technique which greatly improves on the performance of copper cathodes which have a poor QE.

2.5.3 Laser ports design

The oblique incidence angle and laser port diameter limits how small the laser spot size can be. Because our cathode cell has been significantly reduced in length, the oblique incidence angle has been restricted. The current iris design restricts the illumination angle to 12^o. The numerical aperture of the ports is NA=0.083. The calculated beam waist, $w_o = \frac{\lambda_o}{\pi NA}$, is 1μm with a drive laser wavelength, λ_o, of 266nm. With this set-up, the smallest laser spot projection $(w_o/tan(12^o))$ achieved is 5.8μm in size.

Laser port geometry was optimized with HFSS with the same restrictions as the coupling ports in order to maintain a low pulsed heating. All edges have been strongly rounded maintain the $H_{surface} <$ 480kA/m, Fig. 2.28(Left) One of the issues arising from shortening of first cell is the machining these rounded edges and the ability to access these corners. To ease these fabrication challenges, the first cell was truncated to create a surface normal to the laser ports as shown in Fig. 2.28(Right).

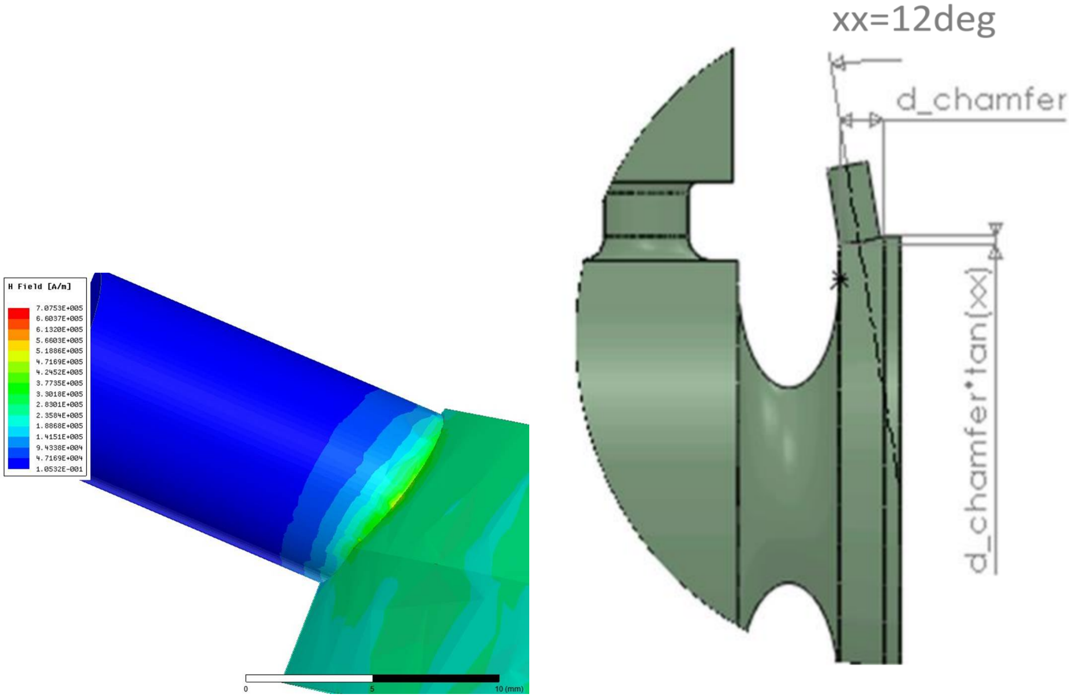

Figure 2.28: (Left)Surface magnetic field of the laser ports.(Right) Cathode cell geometric adaptation for laser ports.

2.5.4 Special cathodes for ultrahigh brightness beam from S-band photoinjector

We have discussed the use of metal cathodes such as copper cathodes and how we have incorporated in our design ways to utilize them for ultra-low emittance beam generation. Improving the MTE of the copper photocathode could technically be down by increasing the emission wavelength but this will reduce the QE.

Advancements in the MTE of photocathodes have been made recently in the semiconductor photocathode materials but mainly on DC electron guns which operate at much lower gradients ($< 10MV/m$), than the RF electron guns. The UCLA photoinjector will also incorporate a cathode loading technique that will allow high gradient testing of semi-conductor cathodes.[53]

Alkali Antimonide cathodes, such as CsK_2Sb, $NaKSb$ amongst other, are of great interest as they have very low MTE (35MeV) [54] [53]. The main disadvantage of AA cathodes is the manufacturing and strict handling of vacuum conditions. These cathodes are fabricated using evaporative deposition. Not only are they grown in vacuum, they must be transported and installed under vacuum. Most electron guns do not have a cathode installation system that allows extracting or inserting photocathodes under vacuum. Typical systems have a cathode plug that requires opening the cathode back flange which exposes the photoinjector to air.

2.5.5 The UCLA load-lock

In order to allow testing of AA cathodes in the high gradient S-band photoinjector we designed a novel load-lock chamber to be compatible with our gun design. The load lock consists of three major sections as shown in figure.

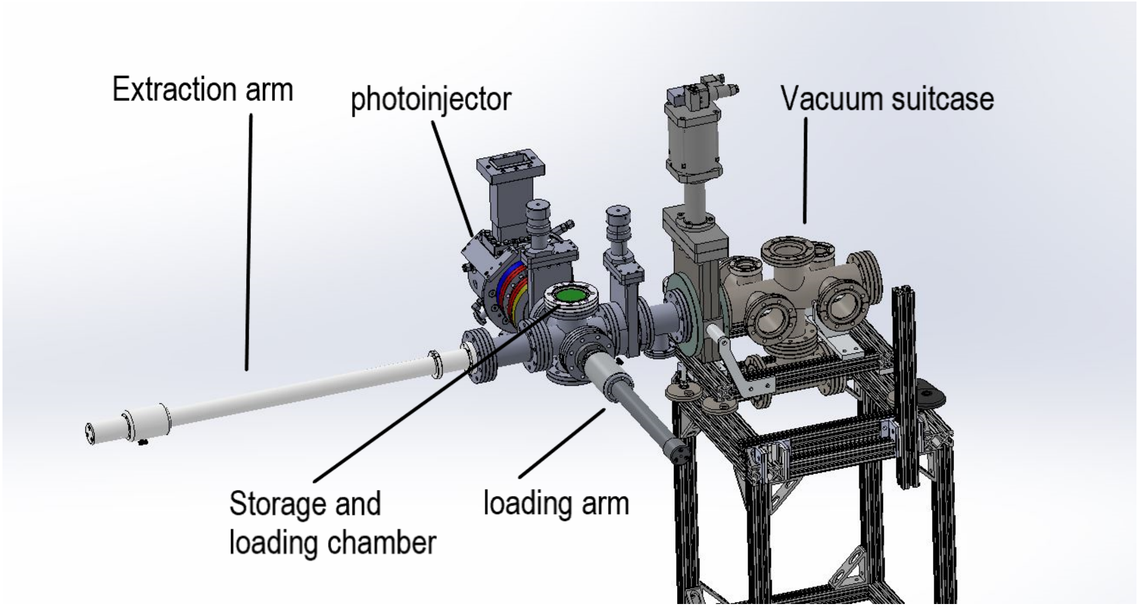

Figure 2.29: Load-lock schematic of main components.

First section:

A vacuum suitcase to house the grown alkali-antimonide special cathodes to be inserted into the photoinjector. The system is designed to maintain the cathodes in ultra-high vacuum (UHV) conditions, below $10^{-}9$ torr. The cathodes are held on the tip of a metal plug and stored inside the suitcase. The plugs are held in a line on a carriage which allows the operator to select the desired cathode. The collaborator for this project is LBNL. They are growing the AA cathodes to operate in their vacuum suitcase. The LBNL suitcase will be shipped to UCLA with the cathode plugs stored inside under UHV. The UCLA load-lock has been designed to work with this suitcase. Radiabeam technologies is also working on the development of another vacuum suitcase system to fit the UCLA load-lock which opens the potential for growing and testing AA cathodes in-house in the future.

Second section:

The second section is the loading chamber. It consists of two arms: a 24” stroke translator arm is used to extract a carriage of special cathodes from the vacuum suitcase and pull the carriage into the main loading chamber (6-way cross).

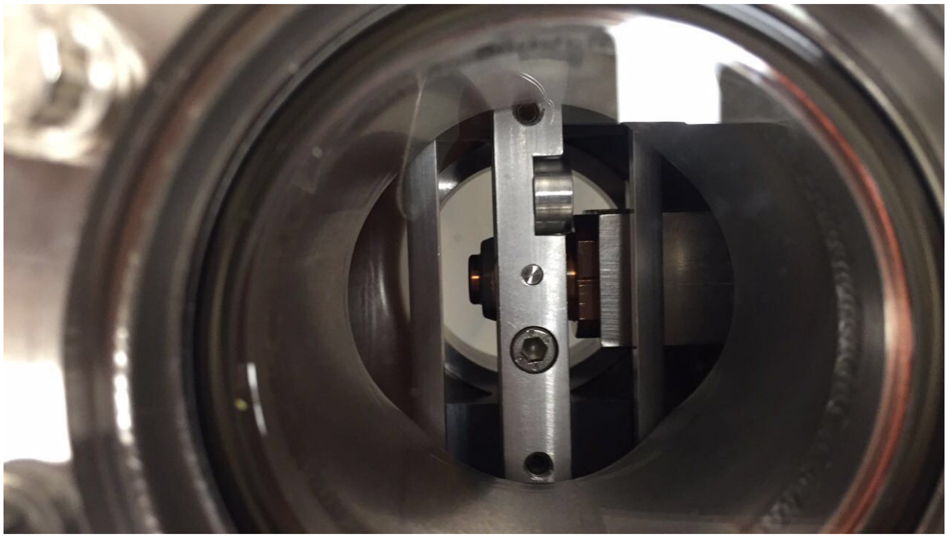

Figure 2.30: Top view of the load=lock chamber with cathode plug.

Third section:

To insert the cathode into the photoinjector, a 12” stroke translator called the loading arm. The loading arm retrieves the cathode plug from the extraction arm and slide the plug into the cathode position inside the RF photoinjector.

The load-lock system has already been assembled at UCLA as of 2018. The 12” and 24” axial stroke, magnetically coupled, translator arm was manufactured by UHV Design and supplied by Kurt J. Lesker. The system has two gate valves: a custom made 4.50” CF valve with a 6.00” CF flange port and a standard 4.50” CF. The main chamber consists of a 6-way 4.50” CF cross. The system has been assembled without the LBNL vacuum suitcase but has started vacuum testing using a NEG pump and two ion pumps. Currently, the system has achieved a vacuum pressure of 10^{-9} torr and working towards even lower vacuum pressure.

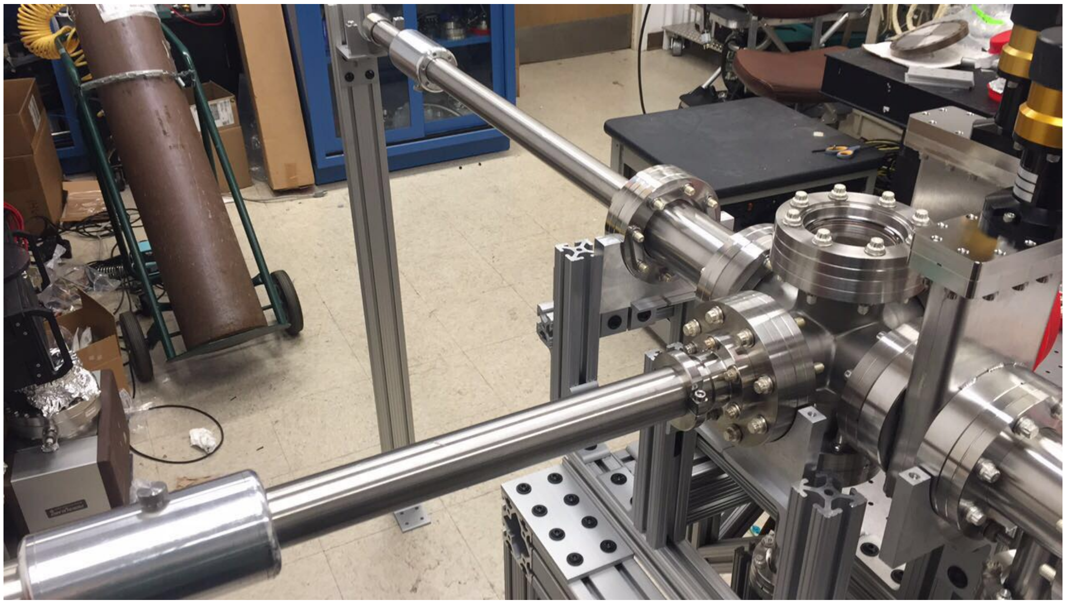

Figure 2.31: Load-lock assembled in a UCLA testing laboratory.

The preliminary design of the cathode back wall for the photoinjector has been designed to accept the cathode plugs from the load-lock as shown in Fig. 2.32. To allow clearance between the cathode back holder and the APEX puck there has to be a tolerance gap between the two parts. The changes in the geometry affect the frequency as it changes the volume of the cavity but, more importantly, there is a risk for field concentration in these small areas which can negatively affect the rf breakdown.

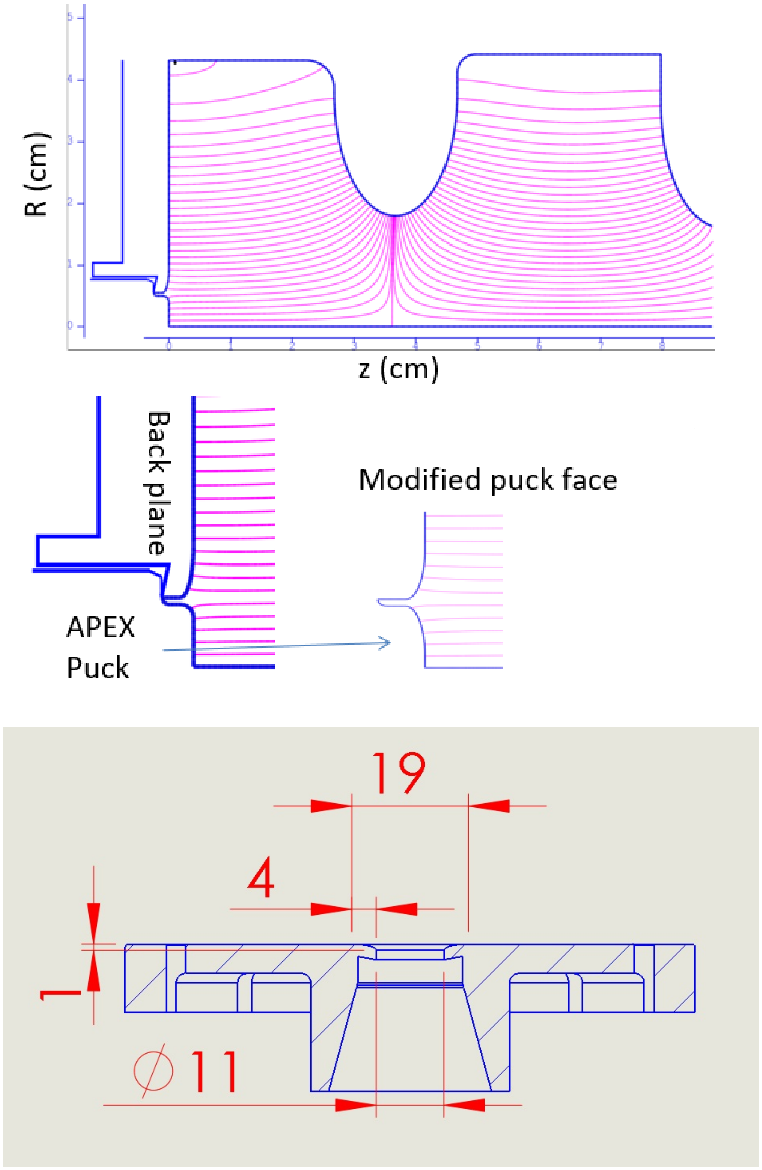

Figure 2.32: Electron gun back wall and receptor for load-lock cathodes. (Top) CAD model. (Bottom) Drawing.

Testing the cathode puck into the 1.6 cell rf photoinjector only showed a 500kHz shift in the resonance frequency which can be compensated by tailoring the operation temperature. Simulations, in SUPERFISH and HFSS, both show a distortion of the field balance to a 75% as shown in Fig. 2.33. For optimal performance the load-lock cathode back receptor will have to be redesigned and effects of small gaps in regions of large fields require further understanding.

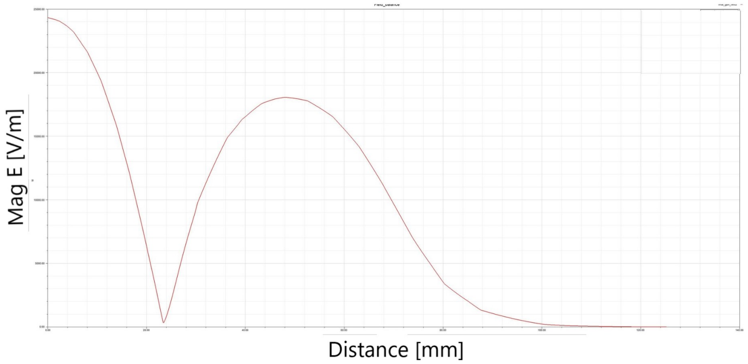

Figure 2.33: HFSS simulations of the effect of the new load-lock cathode back receptor on the field balance.

2.6 Clamping Technique

In the previous section, we discussed the efforts in the cavity geometry design to maintain a low pulsed heating temperature rise to prevent RF breakdowns. In the previous chapter, we covered the limitations that the RF breakdowns imposed on high gradient structures like the 1.4 cell photoinjector and discussed the latest studies on the subject. In Fig. 1.7, it is shown that a harder copper material significantly reduces the RF breakdown observed.

Typical photoinjectors are fabricated using brazing or techniques that involve heat treatment. Brazing has several disadvantages. Brazing is a high risk procedure that is also costly. The process also softens the copper which increases the RF breakdown probability. The LNF-INFN developed a clamping technique for the manufacturing the SPARC 1.6 cell photoinjector to avoid this heat treatment. The clamping technique avoids the brazing process with the help of special gaskets.

Both photoinjectors are machined in parts as shown in fig. 2.6.

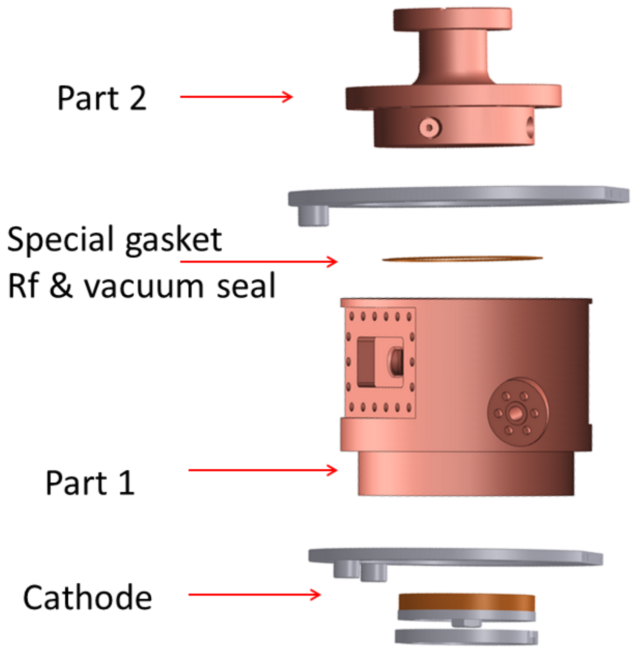

Part 1 contains the cathode cell, iris and full cell. Due to its geometry, it is machined using a five-axis milling machine and diamond tools. The cavity is machined out of a single piece of Oxygen Free High Conductivity (OFHC) copper that has never undergone heat treatments during the stock manufacturing.

Part 2 is a cap that plugs into the full cell. Part 1 and 2 are clamped together using a special gasket that vacuum seals and guarantees RF contact. The SPARC design was adapted as shown in Fig. 2.34 to fit the 1.4 cell full cell racetrack geometry.

Inside the main cavity there is a step for the RF gasket to be placed. The insertion of the cap is the mechanism that compresses the RF gasket and thus creating the rf and vacuum seal. The gap between the cap (once fully inserted) and the face of the

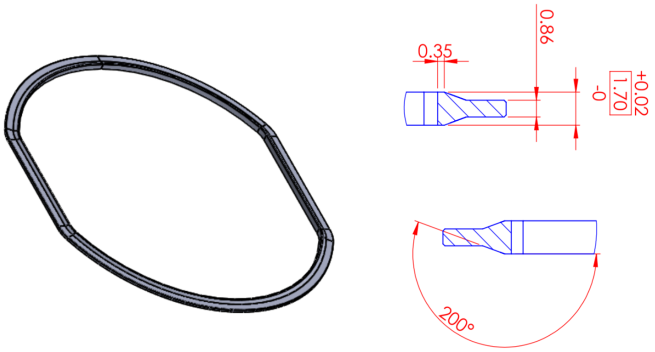

Figure 2.34: Special vacuum and RF gasket to seal Part 1 and cap.

step is the maximum allowed compression for the gasket. The gasket height is 1.7mm. The gap between the cap and the step is 1.45mm allowing the gasket to compress by 0.25mm.

New vacuum sealing gaskets were developed and tested at UCLA to completely avoid any brazing/welding of the external components onto the main body such as the laser and vacuum ports. To facilitate compatibility with commercial available vacuum and beamline components, a gasket design was made to seal act as the interface between the copper body and a standard CF flange. One side of the gasket is flat to allow the knife edge on the CF flange to bite into the gasket[55] while the opposing side contains its own knife edge that digs onto the copper body as shown in Fig. 2.35.

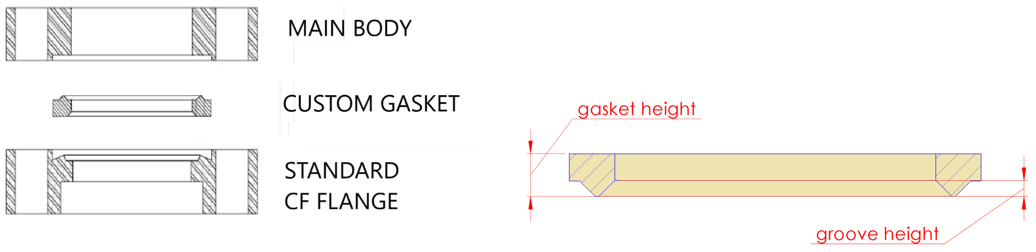

Figure 2.35: Body to conflat (CF) flange clamping elements.

Three gaskets were designed to be compatible with the most commonly used conflat (CF) fitting sizes in accelerating beamlines: DN 16 (1.33”), DN 40 (2.75”) and DN 100 (6”). Cross section schematics are shown in fig. 2.36. The pocket depth on the main body plus the conflat depth determine the final height of the gasket once the parts have been clamped and the gasket is fully compressed. No gap exists between the main body and the CF flange face. The advantage of allowing the pocket depths to determine the compression of the gasket is that it removes the ability to over compress the gasket which could result in a sealing failure.

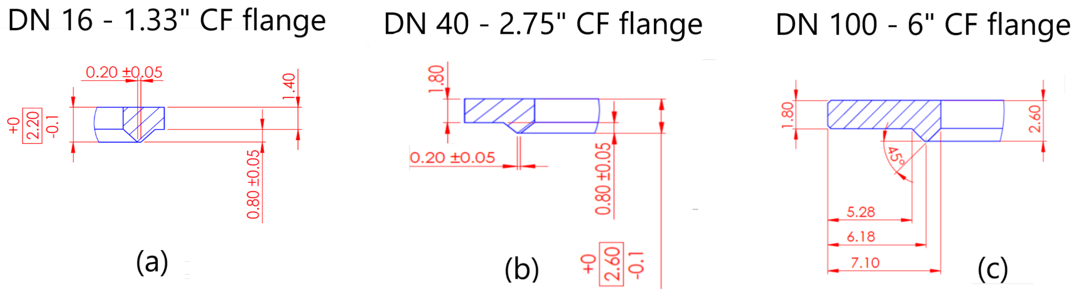
DN 16 - 1.33" CF flange
DN 40 - 2.75" CF flange
DN 100 - 6" CF flange

Figure 2.36: 2D schematics of custom copper to CF gasket cross-sections. (a) DN16. (b) DN40. (c) DN100.

The optimal gasket compression and dimensions of the system are summarized in the following table.

Table 2.3: Custom gasket for CF flanges compression parameters

	DN16	DN40	DN100
Gasket height	2.2	2.6	2.6
Pocket depth	0.8	1.1	1.1
CF depth	1.2	1.2	1.2
Compression	0.2	0.3	0.3

The gaskets were tested by creating a blank copper cap which can be bolted with the commercial standard CF flange and sealed using our custom gaskets. The copper blank contains a pocket with a depth that determines the compression of the knife edge of the gasket. Optimal compression was determined to guarantee contact all around and withstand large temperature fluctuations. The copper blank also contains 0.5 mm radii channels on the surface which provide inlets for helium gas for the leak detection testing. Commercial CF flanges have the same type of channels.

The first vacuum sealing test was the helium leak test. With the three components clamped together, we attached the system to a He leak detector. Using an external helium gas supply, the helium gas was fed into the inlet channels and surrounding regions of the gaskets. The helium detector test was successful and no helium made it inside the system showing the gasket had successfully sealed the gap between the copper blank and CF flange.

The second test carried out was a bake-out procedure which is a standard process for high purity applications and ultra high vacuum systems. The vacuum bake-out is used to remove contaminants that are in the system or have been absorbed by the system components. The procedure involves applying heat to the surface to trigger thermal out-gassing and remove the impurities which are then extracted out by the vacuum pumps[56].

Our system was first put under vacuum at 10^{-8}torr pressure. The system was then wrapped entirely in a layer of foil to distribute the heat across the system. Heating strips with a manual temperature control knob are wrapped above the foil. All the parts that are included in our system can withstand up to $120^{o}C$. During the bake out procedure the copper gaskets can deform due to heat expansion causing the vacuum seal to fail and allowing air to leak inside the chamber. The first gaskets tested failed due to being fabricated out of copper stock that did not meet the hardness criteria to withstand this heat treatment. A Brinell and Rockwell hardness test was performed on the stock and was classified as 'dead' soft. It was found that an OFE HC 101 Copper with a Brinell hardness rating above 50 was necessary. The next set of gaskets were compressed and baked and reached a final vacuum pressure of 5×10^{-9}torr.

A similar approach was taken in the design of the waveguide gasket.The cross section is shown in fig. 2.37.

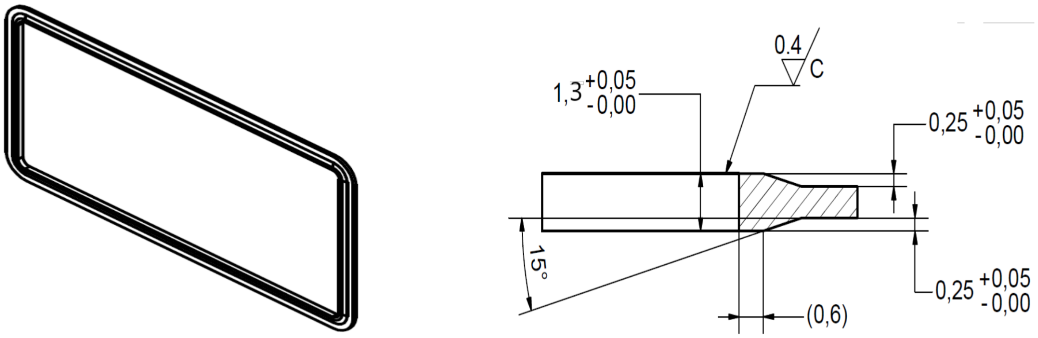

Figure 2.37: 2D schematics of the custom waveguide gasket cross-section

The total height of the gasket is 1.3mm. A groove of 0.95mm was made with a custom made copper waveguide gasket that seals the the coupling port to the standard WR295 rectangular waveguide flange for an optimal compression of 0.35mm.

CHAPTER 3

X-band Deflector

3.1 UCLA X-band deflector

Ultrafast electron diffraction has played a very important role in the measurement of atomic motion and is one of the frontiers of modern science. Because of all the advancement in this field, there are strong demands for even shorter bunches in order to improve the resolution of time-resolved measurements. It is in this framework that a new X-band deflecting cavity is designed and built with the goal to develop an innovative, inexpensive and low energy UED system that takes advantage of the techniques developed for the manufacturing of the 1.4 cell RF photoinjector discussed in chapter 2. The following sections will first give more details about the application, present the beam dynamics needs and finally discuss the electromagnetic design and the fabrication techniques implemented.

3.1.1 Ultrafast Electron Diffraction

Ultrafast electron diffraction has emerged recently as a useful technique for structural dynamics investigation at sub-picosecond temporal resolution. The concept is based on the ability to generate short electron beams from photocathodes using femtosecond laser pulses and then using these bunches to interrogate the structure of a sample at a given delay from a pump laser pulse [57][58].

Extremely short bunches are necessary for this particular application as the length of the electron bunch poses a direct limit on the temporal resolution attainable. Measuring these ultra short beams is a challenge for the technologies available.

Typical current monitors have rise times in the nanosecond range which eliminates them as a diagnostic candidate. Other previously used methods involve making the beam interact with a conducting or refracting material to generate a radiation pulse and extract the time profile information through an optical system (a.g. interferometer). This approach is fundamentally affected by a phase retrieval problem even though reconstruction technique have been proposed and assumptions have to be made about the original profile shape or phase distribution [59] . A popular device for temporal resolution measurement is the streak camera. Using a photocathode for photo-emission and accelerating the electron in a cathode ray tube that "streaks" them transversely by deflecting them with a DC electric field and unto a detector [60]. Streak cameras have been used in the past but the used of such short bunches is well beyond their range. Ultrafast electron diffraction studies are pushing electron bunches of sub-picosecond pulses in the 30-100keV energy range. In this chapter, we will discuss the design of a novel RF deflecting cavity based on the fabrication principles already explored in the 1.4 cell gun project to streak the longitudinal beam distribution of an electron beam in a UED setup to reach the desired temporal resolution[61].

3.1.2 Future UCLA UED experiments

The UCLA X-band deflector will be used as a streak camera to measure the bunch length of a low energy 30 keV electron beam, but it can also play a role in a drastically different approach to temporal resolution measurements. The x-band deflector in fact could also be placed immediately after the sample such that it operates on the diffracted beam. The set-up shown in fig. 3.1 and called Continuously Time Resolved UED has two main advantages.

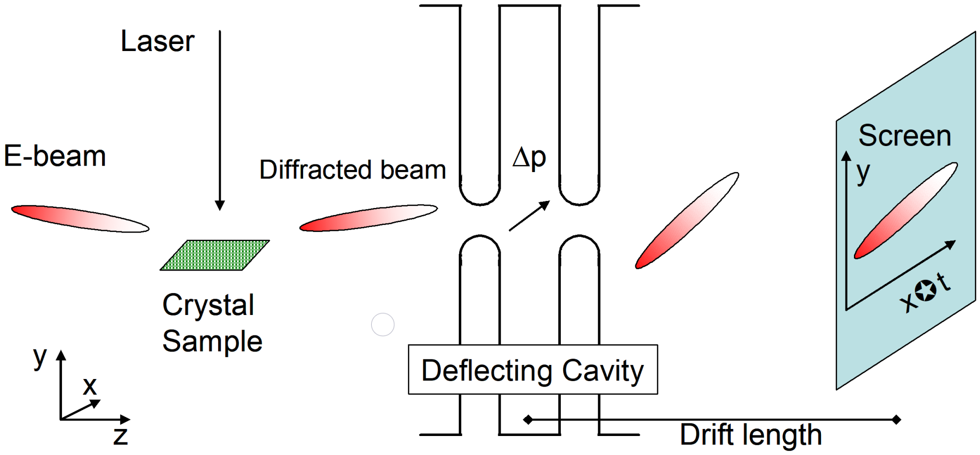

Figure 3.1: UCLA porposed UED system using deflecting cavity on diffracted beam.

The first advantage is that temporal resolution no longer depends in the length of the electron beam. The resolution is now dependent on the RF power, $P_{RF} = \frac{V_0^2}{R_{shunt}}$, where R_{shunt} is the shunt impedance of the cavity. This allows the use of longer electron bunches. We can also take advantage of the power scaling with the resonant frequency as seen in equation [reference equation 1.3]. The use of 9.6 GHz, X-band frequency could potentially allow temporal resolution as fine as 100fs.

The second advantage of the UCLA UED set-up is that we are able to work with longer bunches reducing the tight requirements on the beam charge to be able to generate ultrashort electron beams. For example in a 55keV electron gun, a bunch length of few hundred fs can be obtained only maintaining the number of electrons in the pulse below 1000.

As mentioned before, RF deflecting cavities typically operate in relativistic beamlines which require MV/m peak fields and RF power in the order of MW. This new experiment will use a low voltage (10kV) and manageable RF power (1kW) levels to deflect non-relativistic beams.

3.2 Relevant beam dynamics theory

In Chapter 2, we discussed the design of an RF electron gun. RF photoinjectors typically avoid any fields that steer the beam from the traveling axis. Deflecting cavities are designed with the opposed idea in mind. The electromagnetic field of the mode excited in the cavity is shaped to induce a deflecting voltage and steer the beam away from the traveling axis. The high frequency time variation of the deflecting fields is used to pitch or yaw the electron bunch, where the resulting transverse beam spatial quantities can be correlated with the time structure of the bunch.

Even though the idea of deflecting structures is old, they have been recently re-introduced in modern accelerator and beam physics for new applications[62]. They have primarily been used for particle separation in beams of more than one species and as a longitudinal bunch length diagnostic. New applications have re-introduced deflecting cavities such as longitudinal phase space reconstruction and creation of temporal correlations.

Deflecting cavities create a time-varying transverse deflection of charged particles. It is useful to start with the Lorentz force equation for a particle traveling in the z direction,

$$\vec{F} = q(\vec{E} + \vec{\nu} \times \vec{B}) \tag{3.1}$$

where q is the charge, $\vec{\nu}$ is the velocity, $\vec{E}$ is the transverse electric field and $\vec{B}$ is the transverse magnetic field. In order to provide a kick away from the z-axis, we require to generate a horizontal E field or a vertical B field given that the main beam velocity is along the z-axis.

Looking back at the modes of a pillbox cavity described earlier, we consider the modes TM$_{mnp}$ which vary as $B_r \propto J_m(k_t r) sin(\phi_m)$ and $E_r \propto J_m(k_t r)(cos\phi_m)$ where k_t is the transverse wavenumber. Photoinjectors typically using the monopole mode, TM_{010}, because they have zero transverse fields at r = 0 in order to preserve the beam quality. Deflecting cavities, on the other hand, need to operate in different modes in order to have non-zero kick in the cavity center. Dipole modes can achieve this as they have both transverse electric and transverse magnetic fields at the traveling axis.

We return to the Panofsky Wenzel theorem and write the deflecting voltage, V_x as,

$$V_x = \int \frac{F_x}{q} dz = \int (E_x + (c \times B_y))dz = \frac{-ic}{\omega} \int (\nabla_t E_z))dz \tag{3.2}$$

The deflecting voltage is $\pi/2$ out of phase and proportional to the gradient of E_z [62]. Therefore, modes that do not have longitudinal electric fields (TE modes) are not used for deflecting ultra-relativistic particles. For non relativistic beams it is possible to use also TE modes due to the Lorentz force coupling. For TM modes, the deflection is mostly magnetic. A common mode for deflecting cavity operation is the lowest dipole mode, TM$_{110}$. For relativistic beams, the typical set up of these deflecting cavities operating in the TM_{110} is as shown in the Fig. 3.2, They typically require MV/m peak fields, MW level of RF power.

When an electron bunch with an RMS length , σ_z, enters the deflector it is kicked

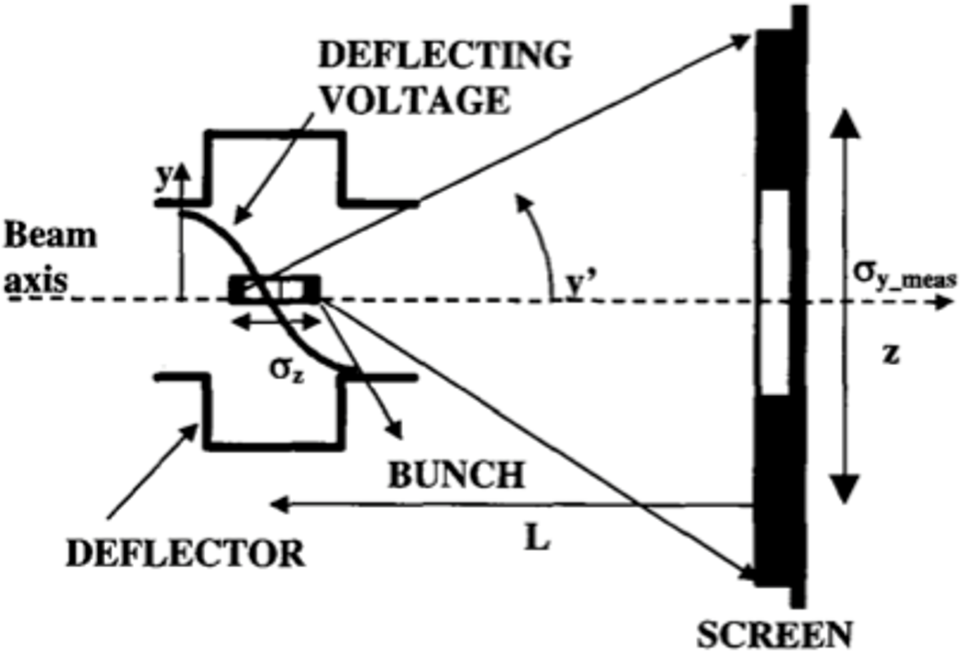

Figure 3.2: 2.75" custom gasket profile.

vertically in the y-direction, in the situation of the schematic in Fig. 3.2. The transverse distribution of the bunch at the screen,$\sigma_{y_{meas}}$, is a convolution of the deflected beam and vertical slices of the bunch at the screen. Its rms transverse extent can be expressed as,

$$\sigma_{y_{meas}} = \sqrt{\sigma_{y0}^2 + \sigma_{def}^2} \tag{3.3}$$

Where σ_{def} is related to the longitudinal size of the beam by

$$\sigma_{def} = \frac{eV_0}{E}\frac{2\pi f}{c}\sqrt{\beta_{yd}\beta_{ys}}|sin(\Delta\Psi)|\sigma_z \tag{3.4}$$

where β_{yd} is the betatron function of the deflector, β_{ys} is the betatron function of the screen, V_0 is the deflecting voltage, $\Delta\Psi$ is the betatron phase advance between the deflector and the screen and $E = pc$ is the energy in eV. The transverse size of the beam when the deflector is off, σ_{y0}, is written as

$$\sigma_{y0} = \sqrt{\frac{\beta_{ys}\epsilon_{ny}}{\beta\gamma}} \tag{3.5}$$

where β and γ are the relativistic factors and ϵ_{ny} is the beam transverse normalized emittance.

An important aspect of these systems is the ability to distinguish the deflected beam from the un-deflected beam which is quantified by the K parameter. The minimum bunch length, $\sigma_{z_{res}}$, that can be resolved along with the K parameter allows to find the minimum deflecting voltage for a simple drift section, $V_{t_{min}}$ the cavity must have

$$eV_{t_{min}} = K\frac{cE}{2\pi f}\frac{1}{L_{cav}}\frac{\sigma_{y0}}{\sigma_{z_{res}}} \tag{3.6}$$

and the minimum attainable temporal resolution can be approximated to, $\Delta t = \sigma_0/K$.

In this project we try to design an X-band cavity (f = 9.6 GHz) capable of streaking a 30 keV electron beam with 100 fs temporal resolution. The required minimum transverse deflection is $4.2keV/\sqrt{kW}$.

In order to maximize the deflecting voltage for a given input power we choose to utilize a reentrant nose cone geometry. The nose geometry allows a higher efficiency to the deflector. Due to the particles not being relativistic, it is important that that the particles exit the cavity before the oscillating RF field changes sign. This effect results in an optimal length for a given beam velocity. This can be written using the transit time factor which can be written as

$$T = \frac{sin(\frac{\pi L}{\beta\lambda})}{\frac{\pi L}{\beta\lambda}} \tag{3.7}$$

in the expression for the total deflecting voltage. The goal is to choose an effective length L that maximizes T, preventing a reduction in the deflection.

3.2.1 Electromagnetic Design

The nose cone X-band deflector was designed using HFSS 3D electromagnetic code. The resonant frequency of the X-band structure is 9.6GHz. This resonant frequency is compatible with the available 50kW peak power Klystron from Radio Research Instruments. This power will be our reference for our fields profile.

The deflector cavity is made out of two main parts that are clamped together, details in the next section. It features a beam entry pipe and an exit pipe, both 4mm in radius. The cavity portion is a nose cone geometry as shown in fig. 3.3. Each part contains identical nose cone shapes. A nose cone geometry geometry helps concentrate the fields toward the center of the deflecting gap thus creating stronger fields and therefore stronger deflection. The nose cone geometries also improve the shunt impedance of by a factor of 10 compared to a standard deflector. The mode separators are 2 small cylindrical holes added to create larger separation of the modes preventing unwanted modes to affect the beam dynamics. A mode separation of 7MHz was achieved.

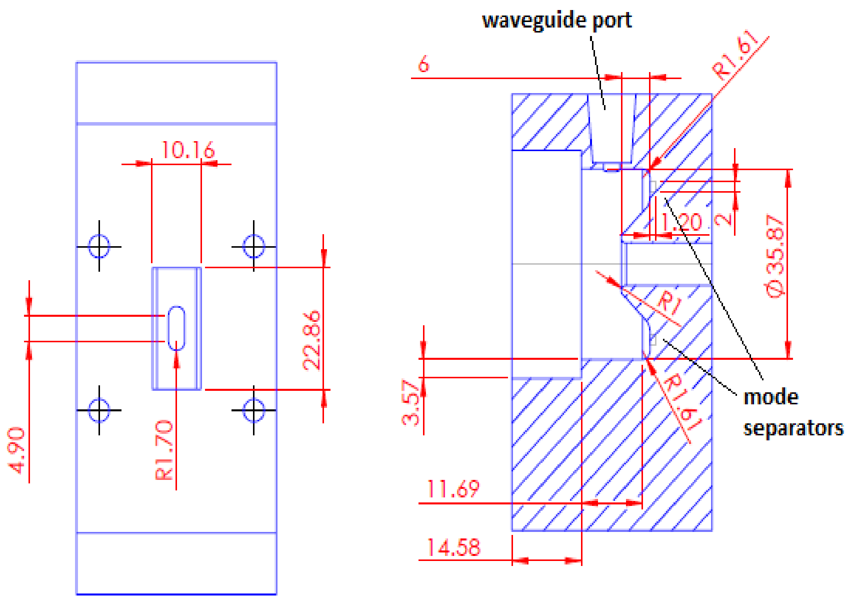

Figure 3.3: Nose cone CAD drawing of Part 1 with dimensions in [mm]

The field profile along the beam axis is shown below in fig. 3.4.

The cavity is coupled to the RF using the side-wall method. The coupling port has a racetrack geometry and uses a WR90 waveguide. Since the power of the cavity is an important parameter to the temporal resolutions is worth redefining some parameters in terms of power. The cavity is driven by the RF power that is externally generated, P_{RF} and can set the temporal resolution. We have plotted the fields using a 50kW Klystron. We know these structures are not lossless systems so we can take a look at distribution of this power. The power lost in cavity is defined as

$$P_{lost} = P_{walls} + P_{coupling} \tag{3.8}$$

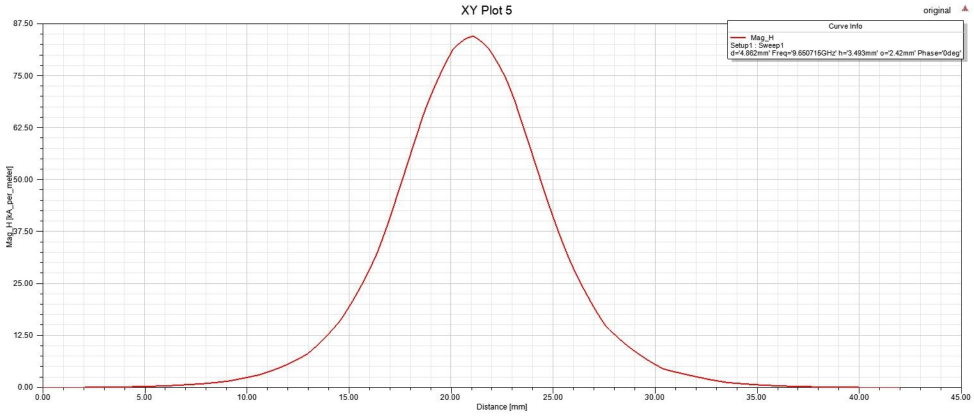

Figure 3.4: On axis magnetic field profile of deflecting cavity with input power of 50kW .

where P_{walls} is the power lost in the walls of the structure and $P_{coupling}$ is the power lost in the coupling port.

We can re-write our quality factors in terms of the power lost as following,

$$Q_e = \frac{\omega_0 U}{P_{coupling}} \tag{3.9}$$

$$Q_0 = \frac{\omega_0 U}{P_{walls}} \tag{3.10}$$

$$Q_{loaded} = \frac{\omega_0 U}{P_{walls} + P_{coupling}} \tag{3.11}$$

The Q_0 of our deflector is 13,400.

As discussed in Chapter 1 [reference coupling section after corrections], we have 3 choices of power coupling where $\beta_{coupling} = P_{walls}/P_{coupling}$. If we drive the cavity in steady state at resonance, then the fraction, $|\Gamma|^2$, of the incident power on the coupler, P_{inc} from the WR90 waveguide will be reflected. Therefore, the power transmitted into the cavity is given by the following expression.

$$P_{walls} = P_{inc}(1 - |\Gamma|^2) \tag{3.12}$$

$|\Gamma|$ has different definitions for the different coupling scenarios.

$$|\Gamma| = \frac{1 - \beta_{coupling}}{1 + \beta_{coupling}}, \text{(undercoupled)} \tag{3.13}$$

$$|\Gamma| = \frac{\beta_{coupling} - 1}{1 + \beta_{coupling}}, \text{(overcoupled)} \tag{3.14}$$

Our structure is critically coupled, $\beta_{coupling} = 1$. Having $P_{walls} = P_{coupling}$ means that the stored energy is being emitted by the coupler at the same rate as the walls are absorbing it. A critically coupled cavity can be driven at steady state means none of the incident power is reflected, P_{ref} and the stored energy is maximized.

In order to find the transverse voltage, the transverse electric field, $\sqrt{E_x^2 + E_y^2}$ along the axis was extracted using the HFSS code. MATLAB was used to perform a polynomial fit of the transverse field and integrate the curve from z=0 to beam exit. For an input power of P=50kW and a frequency of f=9.6GHz, we find the transverse voltage to be $V_T = 8kV$. [63][64].

The transverse voltage is defined as follows:

$$R_{\perp} = \frac{V_t^2}{P} \tag{3.15}$$

.

The transverse shunt impedance is calculated to be $R_{\perp} = 1.3M\Omega$.

A summary of the X-band deflector design parameters have been included in the following table.

Table 3.1: Design parameters for the UCLA X-band deflector

f_π	9.6GHz
Q_o	13,400
Mode Separation	8MHz
$\beta_{coupling}$	1
$R_\perp$	$1.3M\Omega$
V_T at P=50kW	8kV

3.2.2 Clamping technique

In chapter 1, we discussed the detrimental effects on copper cavities caused by Rf breakdowns and Rf pulsed heating temperature rise. In chapter 2, we discussed the design and fabrication techniques that allows us to avoid brazing. 3 different types of sealing gaskets were made. To summarize:

1. RF and vacuum gasket for clamping the cavity body parts.

2. Adapted Conflat (CF) Flange to copper in standard size meant to connect external commercial components to the cavity.

3. Waveguide gaskets that seals standard waveguide components to the coupling port.

Brazing is a risky and an expensive procedure. The customs gaskets proved to be very useful tool for the fabrication of any copper. We have implemented the same fabrication technique on the X-band deflector as we did for the electron gun. In Fig. 3.5, the two main parts that form the cavity are shown. Part 1 and part 2 are clamped together using the custom Rf and vacuum sealing gasket. This gasket features the same profile as seen in fig. 2.35 but with dimensions tailored such that gasket can sit on the pocket inside of Part 2. The X-band deflector has no brazed external components as well. The entry and exit beam pipe have adapted conflat gaskets to be used with commercial 1.33” CF flanges.

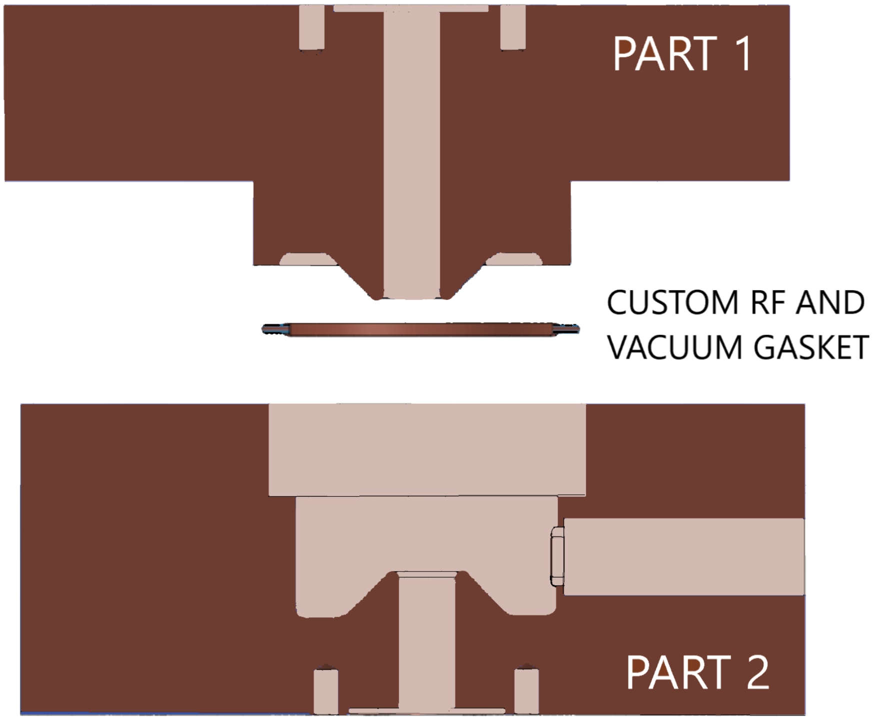

Figure 3.5: The 2 parts and mating gasket of the X-band deflector.

These gaskets are the same design as tested for the 1.4 cell RF photoinjector and results can be found in the ”Fabrication” section of chapter 2.

References

[1] Dennis Thomas Palmer. *The Next generation photoinjector.* PhD thesis, Stanford U., Appl. Phys. Dept., 1998.

[2] P.G. O'Shea, S.C. Bender, D.A. Byrd, B.E. Carlsten, J.W. Early, D.W. Feldman, R.B. Feldman, W.J.D. Johnson, A.H. Lumpkin, M.J. Schmitt, R.W. Springer, W.E. Stein, and T.J. Zaugg. Initial results from the los alamos photoinjector-driven free-electron laser. *Nuclear Instruments and Methods in Physics Research Section A: Accelerators, Spectrometers, Detectors and Associated Equipment*, 318(1):52 – 57, 1992.

[3] J S Fraser, R Sheffield, E R Gray, and P M Giles. Photocathodes in accelerator applications, 01 1987.

[4] R. Ruber, V. Ziemann, T. Ekelf, A. Palaia, W. Farabolini, and R. Corsini. The CTF3 two-beam test stand. *Nuclear Instruments and Methods in Physics Research Section A: Accelerators, Spectrometers, Detectors and Associated Equipment*, 729:546–553, nov 2013.

[5] M. Trigo, M. Fuchs, J. Chen, M. P. Jiang, M. Cammarata, S. Fahy, D. M. Fritz, K. Gaffney, S. Ghimire, A. Higginbotham, S. L. Johnson, M. E. Kozina, J. Larsson, H. Lemke, A. M. Lindenberg, G. Ndabashimiye, F. Quirin, K. Sokolowski-Tinten, C. Uher, G. Wang, J. S. Wark, D. Zhu, and D. A. Reis. Fourier-transform inelastic x-ray scattering from time- and momentum-dependent phonon–phonon correlations. *Nature Physics*, 9(12):790–794, oct 2013.

[6] P. Musumeci, J. T. Moody, C. M. Scoby, M. S. Gutierrez, and M. Westfall. Laser-induced melting of a single crystal gold sample by time-resolved ultrafast relativistic electron diffraction. *Applied Physics Letters*, 97(6):063502, aug 2010.

[7] W. S. Graves, J. Bessuille, P. Brown, S. Carbajo, V. Dolgashev, K.-H. Hong, E. Ihloff, B. Khaykovich, H. Lin, K. Murari, E. A. Nanni, G. Resta, S. Tantawi, L. E. Zapata, F. X. Krtner, and D. E. Moncton. Compact x-ray source based on burst-mode inverse compton scattering at 100 kHz. *Physical Review Special Topics - Accelerators and Beams*, 17(12), dec 2014.

[8] Christoph Bostedt, Sébastien Boutet, David M. Fritz, Zhirong Huang, Hae Ja Lee, Henrik T. Lemke, Aymeric Robert, William F. Schlotter, Joshua J. Turner, and Garth J. Williams. Linac coherent light source: The first five years. *Reviews of Modern Physics*, 88(1), mar 2016.

[9] P. Emma, R. Akre, J. Arthur, R. Bionta, C. Bostedt, J. Bozek, A. Brachmann, P. Bucksbaum, R. Coffee, F.-J. Decker, Y. Ding, D. Dowell, S. Edstrom, A. Fisher, J. Frisch, S. Gilevich, J. Hastings, G. Hays, Ph. Hering, Z. Huang, R. Iverson, H. Loos, M. Messerschmidt, A. Miahnahri, S. Moeller, H.-D. Nuhn, G. Pile, D. Ratner, J. Rzepiela, D. Schultz, T. Smith, P. Stefan, H. Tompkins, J. Turner, J. Welch, W. White, J. Wu, G. Yocky, and J. Galayda. First lasing and operation of an ångstrom-wavelength free-electron laser. *Nature Photonics*, 4(9):641–647, aug 2010.

[10] Tetsuya Ishikawa, Hideki Aoyagi, Takao Asaka, Yoshihiro Asano, Noriyoshi Azumi, Teruhiko Bizen, Hiroyasu Ego, Kenji Fukami, Toru Fukui, Yukito Furukawa, Shunji Goto, Hirofumi Hanaki, Toru Hara, Teruaki Hasegawa, Takaki Hatsui, Atsushi Higashiya, Toko Hirono, Naoyasu Hosoda, Miho Ishii, Takahiro Inagaki, Yuichi Inubushi, Toshiro Itoga, Yasumasa Joti, Masahiro Kago, Takashi Kameshima, Hiroaki Kimura, Yoichi Kirihara, Akio Kiyomichi, Toshiaki Kobayashi, Chikara Kondo, Togo Kudo, Hirokazu Maesaka, Xavier M. Maréchal, Takemasa Masuda, Shinichi Matsubara, Takahiro Matsumoto, Tomohiro Matsushita, Sakuo Matsui, Mitsuru Nagasono, Nobuteru Nariyama, Haruhiko Ohashi, Toru Ohata, Takashi Ohshima, Shun Ono, Yuji Otake, Choji Saji, Tatsuyuki Sakurai, Takahiro Sato, Kei Sawada, Takamitsu Seike, Katsutoshi Shirasawa, Takashi Sugimoto, Shinsuke Suzuki, Sunao Takahashi, Hideki Takebe, Kunikazu Takeshita, Kenji Tamasaku, Hitoshi Tanaka, Ryotaro Tanaka, Takashi Tanaka, Tadashi Togashi, Kazuaki Togawa, Atsushi Tokuhisa, Hiromitsu Tomizawa, Kensuke Tono, Shukui Wu, Makina Yabashi, Mitsuhiro Yamaga, Akihiro Yamashita, Kenichi Yanagida, Chao Zhang, Tsumoru Shintake, Hideo Kitamura, and Noritaka Kumagai. A compact x-ray free-electron laser emitting in the sub-ångstrm region. *Nature Photonics*, 6(8):540–544, jun 2012.

[11] M. Santana Leitner, L. Ge, Z. Li, C. Xu, C. Adolphsen, M. Ross, and M. Carrasco. Studies of radiation fields of LCLS-II super conducting radio frequency cavities. *International Journal of Modern Physics: Conference Series*, 44:1660209, jan 2016.

[12] P. E. Batson, N. Dellby, and O. L. Krivanek. Sub-ångstrom resolution using aberration corrected electron optics. *Nature*, 418(6898):617–620, aug 2002.

[13] R. K. Li and P. Musumeci. Single-shot MeV transmission electron microscopy with picosecond temporal resolution. *Physical Review Applied*, 2(2), aug 2014.

[14] H. Dmer and O. Bostanjoglo. High-speed transmission electron microscope. *Review of Scientific Instruments*, 74(10):4369–4372, oct 2003.

[15] Thomas LaGrange, Geoffrey H. Campbell, B.W. Reed, Mitra Taheri, J. Bradley Pesavento, Judy S. Kim, and Nigel D. Browning. Nanosecond time-resolved investigations using the in situ of dynamic transmission electron microscope (DTEM). *Ultramicroscopy*, 108(11):1441–1449, oct 2008.

[16] P. Musumeci. RF photoinjector based time-resolved MeV electron microscopy. *Microscopy and Microanalysis*, 21(S3):653–654, aug 2015.

[17] Dr. Triveni Rao. *An Engineering Guide to Photoinjectors.* CreateSpace Independent Publishing Platform, 2013.

[18] Luca Serafini and James B. Rosenzweig. Envelope analysis of intense relativistic quasilaminar beams in rf photoinjectors:mA theory of emittance compensation. *Physical Review E*, 55(6):7565–7590, jun 1997.

[19] J.B. Rosenzweig, A.M. Cook, R.J. England, M. Dunning, S.G. Anderson, and Massimo Ferrario. Emittance compensation with dynamically optimized photoelectron beam profiles. *Nuclear Instruments and Methods in Physics Research Section A: Accelerators, Spectrometers, Detectors and Associated Equipment*, 557(1):87 – 93, 2006. Energy Recovering Linacs 2005.

[20] *"Optimization of beam dynamics for an S-band ultra-high gradient photoinjector"*, 2017.

[21] Ernst Ruska. The development of the electron microscope and of electron microscopy. *Reviews of Modern Physics*, 59(3):627–638, jul 1987.

[22] D. Filippetto, P. Musumeci, M. Zolotorev, and G. Stupakov. Maximum current density and beam brightness achievable by laser-driven electron sources. *Physical Review Special Topics - Accelerators and Beams*, 17(2), feb 2014.

[23] J. B. Rosenzweig, A. Cahill, V. Dolgashev, C. Emma, A. Fukusawa, R. Li, C. Limborg, J. Maxson, P. Musumeci, A. Nause, R. Pakter, R. Pompili, R. Roussel, B. Spataro, and S. Tantawi. Next generation high brightness electron beams from ultra-high field cryogenic radiofrequency photocathode sources.

[24] A.D. Cahill, A. Fukasawa, R. Pakter, J.B. Rosenzweig, V.A. Dolgashev, C. Limborg-Deprey, S. Tantawi, B. Spataro, and G. Castorina. RF design for the TOPGUN photogun: A cryogenic normal conducting copper electron gun. *Nuclear Instruments and Methods in Physics Research Section A: Accelerators, Spectrometers, Detectors and Associated Equipment*, 865:105–108, sep 2017.

[25] Evgenya I. Simakov, Valery A. Dolgashev, and Sami G. Tantawi. Advances in high gradient normal conducting accelerator structures. *Nuclear Instruments and Methods in Physics Research Section A: Accelerators, Spectrometers, Detectors and Associated Equipment*, mar 2018.

[26] David P. Pritzkau. *RF pulsed heating*. PhD thesis, Stanford U., Phys. Dept., 2001.

[27] PBPL. Partice beam physics lab, 2018.

[28] National Instruments. Labview, 2018.

[29] David Alesini, Antonio Battisti, Massimo Ferrario, Luca Foggetta, Valerio Lollo, Luca Ficcadenti, Valerio Pettinacci, Sean Custodio, Eylene Pirez, Pietro Musumeci, and Luigi Palumbo. New technology based on clamping for high gradient radio frequency photogun. *Physical Review Special Topics - Accelerators and Beams*, 18(9), sep 2015.

[30] A Giribono, A Bacci, E Chiadroni, A Cianchi, M Croia, M Ferrario, A Marocchino, V Petrillo, R Pompili, S Romeo, et al. Eupraxia@ sparc_lab: the high-brightness rf photo-injector layout proposal. *Nuclear Instruments and Methods in Physics Research Section A: Accelerators, Spectrometers, Detectors and Associated Equipment*, 2018.

[31] Theodoros Argyropoulos, Nuria Catalan-Lasheras, Alexej Grudiev, Gerard Mcmonagle, Enrique Rodriguez-Castro, Igor Syrachev, Rolf Wegner, Ben Woolley, Walter Wuensch, Hao Zha, Valery Dolgashev, Gorden Bowden, Andrew Haase, Thomas Geoffrey Lucas, Matteo Volpi, Daniel Esperante-Pereira, and Robin Rajamki. Design, fabrication, and high-gradient testing of an x -band, traveling-wave accelerating structure milled from copper halves. *Physical Review Accelerators and Beams*, 21(6), jun 2018.

[32] D. Alesini. A vacuum and radio-frequency metal gasket and scturcture incorporating it., 2016.

[33] D. Martin J. Lewandowski V.A. Dolgashev, S.G. Tantawi. Study of rf breakdown in normal conducting cryogenic structure. IPAC 2012.

[34] David Alesini, Antonio Battisti, Massimo Ferrario, Luca Foggetta, Valerio Lollo, Luca Ficcadenti, Valerio Pettinacci, Sean Custodio, Eylene Pirez, Pietro Musumeci, and Luigi Palumbo. New technology based on clamping for high gradient radio frequency photogun. *Phys. Rev. ST Accel. Beams*, 18:092001, Sep 2015.

[35] Marta Csatari Divall, Eduard Prat, Simona Bettoni, Carlo Vicario, Alexandre Trisorio, Thomas Schietinger, and Christoph P. Hauri. Intrinsic emittance reduction of copper cathodes by laser wavelength tuning in an rf photoinjector. *Phys. Rev. ST Accel. Beams*, 18:033401, Mar 2015.

[36] Daniel Velázquez, Rachel Seibert, Hasitha Ganegoda, Daniel Olive, Amy Rice, Kevin Logan, Zikri Yusof, Linda Spentzouris, and Jeff Terry. Tailoring the emissive properties of photocathodes through materials engineering: Ultra-thin multilayers. *Applied Surface Science*, 360:762–766, jan 2016.

[37] Kwang-Je Kim. Rf and space-charge effects in laser-driven rf electron guns. *Nuclear Instruments and Methods in Physics Research Section A: Accelerators, Spectrometers, Detectors and Associated Equipment*, 275(2):201–218, feb 1989.

[38] L.M. Young. Compact photoinjector accelerators for free electron lasers. *Nuclear Instruments and Methods in Physics Research Section B: Beam Interactions with Materials and Atoms*, 56-57:978–981, may 1991.

[39] DESY ZEUTHEN, K Abrahamyan, J Bhr, Ilja Bohnet, V Djordjadze, Ulrich Gensch, H J. Grabosch, Z Li, and D Lipka. First measurements at the photo injector test facility at. 05 2018.

[40] L. Serafini. Micro-bunch production with radio frequency photoinjectors. *IEEE Transactions on Plasma Science*, 24(2):421–427, apr 1996.

[41] Los Alamos National Lab. Superfish.

[42] Ansys. Hfss.

[43] Pulsar. Gpt.

[44] Mathworks. Matlab.

[45] D. Alesini. Power coupling.

[46] W. K. H. Panofsky and W. A. Wenzel. Some considerations concerning the transverse deflection of charged particles in radio-frequency fields. *Review of Scientific Instruments*, 27(11):967–967, nov 1956.

[47] D Alesini, R Boni, G Di Pirro, R Di Raddo, M Ferrario, A Gallo, V Lollo, F Marcellini, L Palumbo, V Spizzo, A Mostacci, G Campogiani, S Persichelli, A Enomoto, T Higo, K Kakihara, T Kamitani, S Matsumoto, T Sugimura, K Yokoyama, and S Verdú-Andrés. The c-band accelerating structures for SPARC photoinjector energy upgrade. *Journal of Instrumentation*, 8(05):P05004–P05004, may 2013.

[48] A Einstein. Indeed, it seems to me that the observations regarding" blackbody radiation," photoluminescence, production of cathode rays by ultraviolet. *Annalen der Physik*, 17:132–148, 1905.

[49] David H. Dowell and John F. Schmerge. Quantum efficiency and thermal emittance of metal photocathodes. *Physical Review Special Topics - Accelerators and Beams*, 12(7), jul 2009.

[50] T Vecchione, I Ben-Zvi, DH Dowell, J Feng, T Rao, J Smedley, W Wan, and HA Padmore. A low emittance and high efficiency visible light photocathode for high brightness accelerator-based x-ray light sources. *Applied Physics Letters*, 99(3):034103, 2011.

[51] Jun Feng, J. Nasiatka, Weishi Wan, Siddharth Karkare, John Smedley, and Howard A. Padmore. Thermal limit to the intrinsic emittance from metal photocathodes. *Applied Physics Letters*, 107(13):134101, sep 2015.

[52] D. Cesar, J. Maxson, P. Musumeci, Y. Sun, J. Harrison, P. Frigola, F. H. O'Shea, H. To, D. Alesini, and R. K. Li. Demonstration of single-shot picosecond time-resolved MeV electron imaging using a compact permanent magnet quadrupole based lens. *Physical Review Letters*, 117(2), jul 2016.

[53] Jared Maxson, Luca Cultrera, Colwyn Gulliford, and Ivan Bazarov. Measurement of the tradeoff between intrinsic emittance and quantum efficiency from a NaKSb photocathode near threshold. *Applied Physics Letters*, 106(23):234102, jun 2015.

[54] L. Cultrera, S. Karkare, H. Lee, X. Liu, I. Bazarov, and B. Dunham. Cold electron beams from cryocooled, alkali antimonide photocathodes. *Physical Review Special Topics - Accelerators and Beams*, 18(11), nov 2015.

[55] E. Pirez, P. Musumeci, J. Maxson, and D. Alesini. S-band 1.4 cell photoinjector design for high brightness beam generation. *Nuclear Instruments and Methods in Physics Research Section A: Accelerators, Spectrometers, Detectors and Associated Equipment*, 865:109–113, sep 2017.

[56] L Holland. Bakeable ultra-high vacuum systems. *Journal of Scientific Instruments*, 39(5):247–247, may 1962.

[57] Ahmed H Zewail. 4d ultrafast electron diffraction, crystallography, and microscopy. *Annu. Rev. Phys. Chem.*, 57:65–103, 2006.

[58] RJ Dwayne Miller. Femtosecond crystallography with ultrabright electrons and x-rays: Capturing chemistry in action. *Science*, 343(6175):1108–1116, 2014.

[59] R. Lai and A. J. Sievers. Determination of a charged-particle-bunch shape from the coherent far infrared spectrum. *Phys. Rev. E*, 50:R3342–R3344, Nov 1994.

[60] G. H. Kassier, K. Haupt, N. Erasmus, E. G. Rohwer, H. M. von Bergmann, H. Schwoerer, S. M. M. Coelho, and F. D. Auret. A compact streak camera for 150 fs time resolved measurement of bright pulses in ultrafast electron diffraction. *Review of Scientific Instruments*, 81(10):105103, oct 2010.

[61] Y. Ding, A. Brachmann, F.-J. Decker, D. Dowell, P. Emma, J. Frisch, S. Gilevich, G. Hays, Ph. Hering, Z. Huang, R. Iverson, H. Loos, A. Miahnahri, H.-D. Nuhn, D. Ratner, J. Turner, J. Welch, W. White, and J. Wu. Measurements and simulations of ultralow emittance and ultrashort electron beams in the linac coherent light source. *Phys. Rev. Lett.*, 102:254801, Jun 2009.

[62] Valery A. Dolgashev, Gordon Bowden, Yuantao Ding, Paul Emma, Patrick Krejcik, James Lewandowski, Cecile Limborg, Michael Litos, Juwen Wang, and Dao Xiang. Design and application of multimegawattX-band deflectors for femtosecond electron beam diagnostics. *Physical Review Special Topics - Accelerators and Beams*, 17(10), oct 2014.

[63] David Alesini, Giampiero Di Pirro, Luca Ficcadenti, Andrea Mostacci, Luigi Palumbo, James Rosenzweig, and Cristina Vaccarezza. RF deflector design and measurements for the longitudinal and transverse phase space characterization at SPARC. *Nuclear Instruments and Methods in Physics Research Section A: Accelerators, Spectrometers, Detectors and Associated Equipment*, 568(2):488–502, dec 2006.

[64] Kenneth B. Mallory. Measurement of shunt impedance of a cavity. *Journal of Applied Physics*, 29(5):790–793, may 1958.